

OBSERVATIONS OF SUPERGRADIENT WINDS IN THE TROPICAL CYCLONE  
BOUNDARY LAYER

A THESIS SUBMITTED TO THE GRADUATE DIVISION OF THE UNIVERSITY OF  
HAWAII AT MANOA IN PARTIAL FULFILLMENT OF THE REQUIREMENTS FOR THE  
DEGREE OF

MASTER OF SCIENCE

IN

METEOROLOGY

AUGUST 2014

By

Shannon L. McElhinney

Thesis Committee:  
Michael M. Bell, Chairperson  
Gary Barnes  
Wen-Chau Lee  
Yuqing Wang

## **Acknowledgments**

I would like to express deep gratitude to Dr. Michael Bell, who has given me indispensable advice and inspiration throughout my two years at UH. The weekly group lunches and two AMS conferences have gone a long way towards getting me where I am today. The optimism and passion of my research group has made these two years fly by. I would like to thank my committee members Dr. Gary Barnes and Dr. Yuqing Wang for their input on my thesis and for guiding me through the graduate TC class, where I learned most of what I know about TCs. I would also like to thank my committee member Dr. Wen-Chau Lee for the radar training during the HERO field project and advice on my thesis.

The graduate students in the UH meteorology department have made the transition to graduate school and living in a new place much easier. This friendly group is always willing to help or just hang out. Lastly, I would like to thank my supporting parents, sisters, and fiancé for always being there from afar.

## Abstract

Secondary eyewall formation (SEF) impacts tropical cyclone (TC) intensity and structure, but the inner core dynamics of this phenomenon are not well understood. Numerical models suggest that a supergradient jet at the top of the TC boundary layer (TCBL) associated with boundary layer convergence and forcing of deep convection may play a critical role in SEF. There is a lack of consensus on the importance and magnitude of supergradient jets, due in part to limited high-resolution observations near the surface. A new spline-based, 3D variational analysis technique called Spline Analysis at Mesoscale Utilizing Radar and Aircraft Instrumentation (SAMURAI) is used to combine airborne Doppler radar, GPS dropwindsonde, and in situ flight level observations to estimate the magnitude of the supergradient wind (SGW). A detailed error analysis is presented for wind, pressure gradient, and SGW retrievals using synthetic observations in the primary eyewall of a Weather Research and Forecasting Model (WRF) simulated Hurricane Rita (2005). The new methodology is then used to examine the SGW in the primary and secondary eyewalls of the real Hurricane Rita on 22 September. Hurricane Rainband and Intensity Change Experiment (RAINEX) field campaign observations from two aircraft are used to estimate the magnitude of the SGW for the northern quadrant of the TC and for the azimuthal average.

Results from the simulated primary eyewall show the methodology is successful at retrieving the tangential and radial wind fields with low errors. The pressure gradient field has a higher error, especially when dropsondes were included in the analysis. The resulting SGW magnitudes are negatively affected by the pressure gradient errors, resulting in unrealistic supergradient maxima near the surface. The root mean square error in the retrieved SGW is  $\sim 5 \text{ m s}^{-1}$ , consistent with an analytic error analysis. The results from the real observations provide new estimates of the magnitude of SGW in mature primary and secondary eyewalls. The primary eyewall was found to have a SGW maximum of  $22 \text{ m s}^{-1}$  (29%) and the secondary eyewall was found to have a SGW maximum of  $16 \text{ m s}^{-1}$  (21%) for the axisymmetric analysis. The new methodology shows promise to estimate SGW and quantify its importance in TCBL dynamics and SEF, but additional error analysis is necessary to refine the estimates.

## Table of Contents

Acknowledgments.....	ii
Abstract.....	iii
List of Tables.....	v
List of Figures.....	vi
1. Introduction.....	1
1.1 Background.....	1
1.2 Previous Studies.....	3
1.2.1 The role of the BL in SEF.....	3
1.2.2 Numerical modeling studies.....	4
1.2.3 Observational studies.....	5
1.3 Goals.....	7
2. Data and Methodology.....	7
2.1 Gradient Wind Calculation.....	7
2.2 Hurricane Rita (2005).....	11
2.3 WRF Simulation.....	12
2.4 Instrumentation.....	13
2.4.1 RAINEX Data.....	13
2.4.2 Synthetic Data.....	15
2.5 SAMURAI.....	17
3. Simulated Primary Eyewall.....	20
3.1 Wind Analysis.....	20
3.2 Pressure Gradient Analysis.....	24
3.3 Supergradient Wind Analysis.....	25
3.4 Axisymmetric Analysis.....	26
4. Real Primary and Secondary Eyewall.....	28
4.1 Wind Analysis.....	28
4.2 Pressure Gradient Analysis.....	29
4.3 Supergradient Wind Analysis.....	30
4.4 Axisymmetric Analysis.....	30
5. Conclusion and Discussion.....	32
5.1 Interpretation of Results.....	33
5.2 Future Work.....	37
6. References.....	38

## List of Tables

Table 1. The tangential and radial wind retrieval error analysis given as root mean square error (RMSE) in  $\text{m s}^{-1}$  as last 2 columns. The first 5 columns show the swath width of data taken to get Doppler velocity from radar, where “x” means the variable used in that “test” run. The 6<sup>th</sup> column shows if synthetic radar data was included, columns 7-9 show the horizontal dropsonde resolution, the 10<sup>th</sup> column shows if the flight level data was included. Each row is a different SAMURAI analysis run.

Table 2. RMSE values, similar to Table 1, for different quadrants of the simulated storm. It includes the wind, pressure gradient, and SGW error analysis for 19 UTC 20 September.

## List of Figures

- Figure 2.1. The National Hurricane Center best-track positions for Hurricane Rita from 18 to 26 September, 2005.
- Figure 2.2 The WRF simulation intensity compared to the best track intensity data for Hurricane Rita over the 84 hours simulation period.
- Figure 2.3 Evolution of the dBZ field in the WRF simulation in 6-hour intervals from 20 September 00 UTC to 21 September 06 UTC.
- Figure 2.4 The tracks of the N42 and NRL aircraft at approximately 18 UTC 22 September in the northern part of Rita, overlain on radar reflectivity (from Bell et al. 2012b).
- Figure 2.5 A schematic demonstrating the Dual Doppler wind retrieval from the fore and aft beams of an airborne Doppler tail radar.
- Figure 2.6 Real (a) and synthetic (b) edited radar data in NCAR Solo II software. The dBZ field (top) and Doppler velocity (bottom) are shown in a radius height cross-section. The central dot is the location of the aircraft.
- Figure 2.7 (a) The azimuthally averaged radial location of dropsondes and in situ flight level observations used from RAINEX. There are data gaps from 35 to 38 km and inward of 10 km. (b) Dropsondes released during missions on 21 (red) and 22 (blue) September (from Bell et al. 2012b). The blue lines show dropsondes used in this study.
- Figure 2.8 WRF dBZ field during 19 UTC on 20 September with simulated flight track for north leg (black arrow).
- Figure 2.9 The agradient wind retrieval for a Rankine vortex in gradient balance.
- Figure 3.1 The tangential (color) and radial (black lines) “truth” wind field from SAMURAI (a) as a radius-height cross-section. The bold black line indicates where radial wind is  $0 \text{ m s}^{-1}$ , dashed lines are inflow and solid lines are outflow. The retrieved wind field (b) uses only synthetic radar data in SAMURAI from the north leg at 19 UTC.
- Figure 3.2 RMSE plotted with height for V (a) and U (b). The green lines show the RMSE for retrievals using only radar data. Red lines show the RMSE for retrievals using radar, dropsondes, and in situ flight level observations. Note that x-axes are different ranges and intervals.
- Figure 3.3 SAMURAI output for the “truth” pressure gradient of the north leg (a). Test SAMURAI output for the retrieved pressure gradient (b) using in situ flight level data.
- Figure 3.4 Analytic gradient wind speed as a function of radius (km) and radial pressure gradient ( $\text{hPa km}^{-1}$ ). The gradient wind speed is capped at  $100 \text{ m s}^{-1}$  for clarity.
- Figure 3.5 Analytic gradient wind speed error (%) as a function of pressure gradient and pressure gradient error ( $\text{hPa km}^{-1}$ ).
- Figure 3.6 SAMURAI output for the “truth” (a) and “test” (b) SGW field of the north leg at 19 UTC.
- Figure 3.7 Similar to Figure 3.1. Axisymmetric “truth” (a) and “test” (b) wind fields from SAMURAI.
- Figure 3.8 Similar to Figure 3.3. Axisymmetric “truth” (a) and “test” (b) pressure gradient field at 19 UTC.

- Figure 3.9 Similar to Figure 3.6. Axisymmetric “truth” (a) and “test” (b) SGW field from SAMURAI output. The “test” SGW using both flight level and dropsonde data (c) has been included for comparison.
- Figure 4.1 Wind fields from north leg SAMURAI tests using RAINEX observations at 18 UTC 22 September. Tangential wind (color) and radial wind (black lines) were retrieved using only the N42 radar (a), the N42 radar, in situ flight level, and dropsondes (b), and quad-Doppler analysis (c) including ELDORA radar data. The bold black line indicates where radial wind is  $0 \text{ m s}^{-1}$ , dashed lines are inflow and solid lines are outflow.
- Figure 4.2 Radius-height cross section of retrieved pressure gradient ( $\text{hPa km}^{-1}$ ) for the real storm from the north leg.
- Figure 4.3 Radius-height cross section of retrieved agradient wind ( $\text{m s}^{-1}$ ) for the real storm north leg.
- Figure 4.4 Axisymmetric retrieved tangential (color) and radial (contours) winds, from the SAMURAI test using radar, in situ flight level, and dropsonde data from the N42 and NRL aircraft. The bold black line indicates where radial wind is  $0 \text{ m s}^{-1}$ , dashed lines are inflow and solid lines are outflow.
- Figure 4.5 Retrieved axisymmetric pressure gradient ( $\text{hPa km}^{-1}$ ) from N42 in situ flight level observations from the south and north legs.
- Figure 4.6 Axisymmetric SGW from 18 UTC 22 September. Pressure gradients were retrieved using the flight level in situ and dropsonde data (a) and flight level in situ data only (b).
- Figure 4.7 Axisymmetric (a) tangential wind (color) and (b) radial wind (color). Axisymmetric SGW is contours in  $4 \text{ m s}^{-1}$  intervals. The bold black line indicates where SGW is  $0 \text{ m s}^{-1}$ , dashed lines are subgradient and solid lines are supergradient.
- Figure 4.8 Pressure with radius from north and south leg flight level in situ observations (red), axisymmetric SAMURAI analysis pressure (blue), and axisymmetric pressure retrieved using the cubic polynomial method (black dashed). The box on the lower right has the equation and some statistics for the cubic polynomial fit.

# **1. Introduction**

## **1.1 Background**

Eyewall replacement cycles (ERC) are not a common phenomenon, but they drastically change the structure and intensity of some of Earth's most powerful tropical cyclones (TCs). An ERC begins with secondary eyewall formation (SEF) and a subsequent contraction and strengthening of the secondary eyewall as the primary eyewall weakens and is eventually replaced. ERCs have been observed in 80% of TCs with maximum intensities  $>120$  kts in the western north Pacific (Hawkins et al. 2006). The inner core dynamics associated with ERCs are not well understood but may be a key to improving TC intensity forecasts. Recently TC research has focused on TC boundary layer (TCBL) phenomena such as gradient wind imbalance as being important for TC evolution. Several studies suggest a supergradient jet at the top of the boundary layer plays an important role in TC spin-up and SEF (Huang et al. 2012; Abarca and Montgomery 2013) as will be explained later. To the author's knowledge no observations of supergradient wind (SGW) during SEF have been presented in the literature.

TCs are generally assumed to be in gradient balance, with a three-way force balance between the pressure gradient, Coriolis and centrifugal forces. An exception to this assumption is within the TCBL, where the frictional force must be added to the balance. Turbulent fluxes and friction near the surface cause a slowing of the tangential wind and a resulting decrease in the Coriolis and centrifugal forces. The pressure gradient force is sustained so the low-level wind vector points inwards, toward low pressure. The height of the TCBL increases as distance from the center increases



(Ooyama 1982) but is usually within 500 to 1,000 m above the surface in the inner core. For this study the dynamic BL top is defined as the height where inflow is reduced to 10% of the maximum radial wind and eddy momentum fluxes approach zero (Zhang et al. 2011). The axisymmetric boundary layer top was found to be around 1 km for Hurricane Rita (Bell et al. 2012a), however the height may vary considerably around the storm (Sitkowski and Barnes 2009).

The flow is considered out of gradient balance when there is acceleration in the radial direction. Subgradient flow is accompanied by an increase in inflow as the pressure gradient force exceeds the centrifugal force. Supergradient flow is accompanied by a decrease in radial inflow due to an increase in the centrifugal force. A supergradient jet is a well-defined region of increased tangential wind that is believed to exist near the top of the TCBL in intensifying eyewalls. Some BL models indicate the jet is 10-25% greater than the local gradient wind (Kepert 2001). Other numerical models produce larger jet magnitudes (Smith and Vogl 2008). Observations suggest wind speeds that range from a few  $\text{m s}^{-1}$  supergradient (Kepert 2006) to significantly supergradient (Montgomery et al. 2013). The errors and uncertainties associated with the instrumentation and methodology makes it difficult to determine if the jet is a significant feature in real TCs. It is important to quantify the magnitude of this jet and how it evolves with intensifying TCs, through observations, to understand the BL dynamics. Including TCBL processes in operational models should increase the skill of intensity forecasts by improving the prediction of the timing and preferred location of SEF (Huang et al. 2012; Williams et al. 2013; Zhang et al. 2011).

## **1.2 Previous Studies**

### **1.2.1 The Role of the TCBL in SEF**

TCs can intensify through balanced dynamics by adding heat or momentum sources. Latent heating in the eyewall drives a secondary circulation that radially convergenced absolute angular momentum (AAM), which is conserved above the boundary layer. The convergence of AAM causes an expansion of the tangential wind field, increasing the size of the vortex. A recently proposed intensification mechanism includes unbalanced dynamics (Smith et al. 2009). The balanced and unbalanced mechanisms were applied to SEF in three structural steps by Wu et al. (2012) and Huang et al. (2012). The first step is the broadening of the tangential wind field above the boundary layer with the radial convergence of conserved AAM. The second step is the resulting increase in boundary layer inflow outside of the primary eyewall. Inflow is strengthened in the TCBL because the increased tangential wind field means the frictional force becomes proportionally stronger. The stronger inflow enhances inward advection of AAM within the boundary layer. Some AAM is lost to the sea surface and therefore it is not materially conserved. However, spin-up can occur if AAM is advected inward quickly enough at decreasing radii. The third step is the development of a SGW at the top of the BL. Supergradient flow may exist in the BL if the rate of radial convergence of AAM exceeds the rate at which it is lost to the sea surface. The local gradient imbalance causes an outward acceleration leading to an abrupt decrease in inflow and convergence below the supergradient jet. Enhanced low-level convergence in a favorable environment can help sustain deep convection at the radius of the jet. If the

jet is persistent, it can effectively diminish the inner eyewall's inflowing AAM, while contributing to intensification and contraction of a secondary eyewall (Huang et al. 2012).

The TCBL's role and the processes that initiate SEF are still unclear. In fact, the TCBL may not play an essential role in SEF, but acts to enhance the intensification and contraction of the eyewall. Kepert (2013) suggested that once SEF begins, the BL sets up a positive feedback with frictional convergence and convection leading to further intensification.

### **1.2.2 Numerical Modeling studies**

Many numerical modeling studies of the TCBL use a slab boundary layer model (Smith and Vogl 2008; Williams et al. 2013), which is two-dimensional and barotropic. Some recent studies include full physics three-dimensional (3D) models (Wu et al. 2012) or both types of models (Abarca and Montgomery 2013). Abarca and Montgomery (2013) used a full physics model to force a slab boundary layer model at the top and concluded that the slab boundary layer model's unbalanced dynamics played a quantitatively important role in the intensification and contraction of the secondary eyewall. However, another recent study (Menelaou et al. 2014) was able to simulate SEF using a nonlinear 3D model without BL dynamics. When only BL dynamics were used in the model, frictional spin down and no SEF was observed. Their findings support the argument from Kepert (2013), that the TCBL contributes to, but does not initiate SEF.

Kepert and Wang (2001) developed a dry hydrostatic, high-resolution numerical TCBL model, including the full set of primitive equations. They included nonlinear

processes and the vertical advection term to test four storms with varying maximum wind speed, peakedness of the tangential wind radial profile and translation speeds. The model showed that all three variables affect the strength of the supergradient jet. It was also concluded that the jet could sustain itself mainly by vertical advection and diffusion. Above the jet, weak outflow is maintained by the gradient imbalance and supergradient momentum is transported upward in the updrafts and exits the inner core. This allows for a return to gradient balance above the jet. Compared to the linear model (Kepert 2001), the SGWs were stronger when vertical advection was accounted for. Similar jet magnitudes were found in a nonlinear TCBL model developed by Foster (2009).

### **1.2.3 Observational studies**

Numerical models have been useful in studying the dynamics of the data-poor TCBL region, leading to many theories on how TC-scale structure and intensity changes. However, results from numerical models cannot be validated without using real observations from the TCBL. Unfortunately, kinematic and thermodynamic fields with adequate spatial resolution to resolve TCBL features are difficult to obtain due to limitations in our observation capabilities.

The supergradient jet has been observed in several storms using dropsonde measurements (Kepert 2006a; Bell et al. 2012a; Sanger et al. 2014; Didlake and Houze 2011; Zhang et al. 2001). Dropsondes are relatively few and far between so observational studies must make some simplifications and assumptions. Bell and Montgomery (2008) fit dropsonde pressure observations to an azimuthally averaged third degree polynomial curve. The third degree polynomial fit has been used in several recent

studies as well (Didlake and Houze 2011; Bell et al. 2012a; Montgomery et al. 2013; Sanger et al. 2014).

Bell and Montgomery (2008) diagnosed the agradient wind in Hurricane Isabel (2003) using a cubic polynomial fit method. The observed axisymmetric pressure gradient was calculated by averaging dropsonde data in bins (10 km radial, 50 m vertical). The pressure gradient was fit to a cubic polynomial to get the analytic derivative. A radially simplified gradient wind was calculated from the cubic polynomial, resulting in a quadratic shape. They found a 15% SGW in the TCBL near Isabel's RMW, with a quick change to subgradient flow radially outward of 20 km. Although this method produces meaningful estimates of agradient wind at small radii, they admit the quadratic gradient wind profile drops off too quickly at outer radii. It is preferable not to use the cubic polynomial fit to determine the SGW in secondary eyewalls since a secondary maximum in the simplified gradient wind profile is not possible.

The Willoughby et al. (2006) parametric profile has also been used to fit pressure observations (Kepert 2006a, b). Kepert (2006a, b) used two methods to diagnose agradient flow in the TCBL. A pressure analysis of dropsonde data using the parametric profile and radial integration of the gradient wind equation was compared to wind observations. Then a similar wind analysis was independently compared to pressure observations. Hurricane Mitch (1998) was found to have a jet that was estimated to be 5 to 10 m s<sup>-1</sup> supergradient. The wind was found to be most supergradient at the radius of maximum winds, where the tangential wind profile is most peaked, and at 0.5 to 1 km altitude (Kepert 2006b). A similar analysis did not find a supergradient jet in Hurricane

Georges (1998), however that was speculated to be due to the slower decrease in tangential wind with increasing radius (Kepert 2006a). Like the cubic polynomial method, the parametric profile is difficult to use with a double eyewall structure.

### **1.3 Goals**

This study uses a new spline-based variational analysis technique to investigate the degree to which the supergradient jet can be measured in the TCBL with current observational capabilities. It is hoped that this methodology will have an advantage over studies that use the polynomial or parametric fits for TCs with a secondary eyewall. Two cases are presented; the simulated primary eyewall case uses synthetic data to perform a rigorous error analysis, and the real primary and secondary eyewall case applies the methodology to observations from Hurricane Rita (2005). Rita was chosen because of the well-sampled ERC that occurred on 22 September. Three aircraft were collecting observations in Rita for the Hurricane Rainband and Intensity Change Experiment/NOAA Intensity Forecasting Experiment (RAINEX/IFEX) field campaigns. This study attempts to answer the following questions:

- What is the uncertainty associated with retrieving the SGW through synthetic observations?
- What is the magnitude of the SGW in Hurricane Rita's primary and secondary eyewalls and how does it evolve throughout the Rita's lifecycle?

## 2. Data and Methodology

### 2.1 Gradient Wind Calculation

To diagnose the SGW in Hurricane Rita both a wind and pressure analysis had to be done. The pressure gradient was retrieved from in situ flight level observations and used to calculate the gradient wind. The SGW can be determined by comparing the wind field, retrieved from radar, in situ flight level and dropsonde observations, with the calculated gradient wind field.

The gradient wind equation can be derived in natural coordinates (Holton, 2013), where  $\mathbf{t}$  is directed parallel to the horizontal flow,  $\mathbf{n}$  is directed normal to the horizontal flow, and  $\mathbf{k}$  is pointing vertically upward. The Coriolis force in this framework is

$$-f\mathbf{k} \times \mathbf{V} = -fV\mathbf{n} \quad (1)$$

where  $f$  is the Coriolis force,  $\mathbf{V}$  is the horizontal velocity ( $\mathbf{V} = V\mathbf{t}$ ) and  $V$  is a non-negative scalar ( $V = Ds/Dt$ ). The pressure gradient force is

$$-\nabla_p \Phi = -\left(\mathbf{t} \frac{\partial \Phi}{\partial s} + \mathbf{n} \frac{\partial \Phi}{\partial n}\right) \quad (2)$$

where  $\Phi$  is geopotential height. The horizontal momentum equation normal to the direction of flow can be expressed as

$$\frac{V^2}{R} + fV = -\frac{\partial \Phi}{\partial n} \quad (3)$$

where  $R$  is the radius of curvature following the parcel motion. In this study, the force balance parallel to the direction of flow is not included.

The SAMURAI analysis uses cylindrical polar coordinates  $(r, \theta, z)$ , where  $r$  is radius (m) from storm center,  $\theta$  is azimuth ( $^\circ$ ), and  $z$  is height above the surface (m). The radial momentum equation can be written as

$$\frac{\partial u}{\partial t} + \left( u \frac{\partial}{\partial r} + \frac{v}{r} \frac{\partial}{\partial \theta} + w \frac{\partial}{\partial z} \right) u = \frac{v^2}{r} + f v - \frac{1}{\rho} \frac{\partial p}{\partial r} \quad (4)$$

where  $u$  is the radial wind velocity,  $v$  is the tangential wind velocity,  $w$  is vertical velocity,  $\rho$  is the air density, and  $p$  is the atmospheric pressure.

If the radial flow is small compared to the tangential wind, then the total wind speed can be approximated by the tangential wind alone, and the cylindrical coordinate system is approximately a natural coordinate system for the flow. Under this assumption the flow is in gradient wind balance if there is no radial acceleration and the left hand side of Eq. 4 is zero. Therefore in a cylindrical coordinate system gradient wind balance can be written as:

$$\frac{v_g^2}{r} + f v_g = \frac{1}{\rho} \frac{\partial p}{\partial r}.$$

Here  $v_g$  is the gradient wind and can be solved for using the quadratic equation

$$v_g = -\frac{fr}{2} \pm \sqrt{\frac{fr^2}{2} + \frac{r}{\rho} \frac{\partial p}{\partial r}}. \quad (6)$$

For this to have a physical solution in a cyclonically rotating low-pressure system, both  $v_g$  and  $\frac{\partial p}{\partial r}$  must be positive. Then the agradient wind is simply

$$v_{ag} = v - v_g \quad (7)$$

where  $v_{ag}$  is agradient wind and  $v$  is retrieved tangential wind. If agradient wind is positive there are SGW and where it is negative there are subgradient winds.



A script was created to do the SGW calculation and it was first tested on a Rankine vortex in gradient wind balance. Figure 2.10 shows that the calculated gradient wind is nearly identical to the tangential wind; therefore the SGW is zero. There is a small difference due to some smoothing from the cubic B-spline near the peak tangential wind, where the Rankine vortex wind field is discontinuous.

According to Brill (2014) there are four different ways to define the gradient wind: steady contour, non-steady contour, steady natural, and non-steady natural. Diagnosing SGW depends on which definition is used. In fact, for the non-steady natural gradient wind it is not possible to have SGW, but this gradient wind defines the upper bound for the actual wind speed. The definition used in this study, as in many previous TC studies, is the steady contour gradient wind. “Steady” means there is no change in the radius of curvature with time, while “contour” means the radius of curvature ( $R$ ) used in Equation 3 follows the streamlines of the geostrophic wind instead of the streamlines of the actual wind.

In the analysis, gradient balance was analyzed first on a leg-by-leg basis and then on the azimuthal mean (axisymmetric) vortex. The northern leg and axisymmetric analyses are shown in the results section, but the southern, eastern and western legs were also analyzed. It remains unclear if gradient balance is a practical assumption for a small fraction of the storm. In fact, there is no observational or theoretical reason to expect gradient balance exists in one quadrant of the TC (Willoughby 1990). Part of the motivation for analyzing the northern leg was to see if similar gradient features exist in both the single leg and axisymmetric analysis. Many previous studies, such as those mentioned in Chapter 1.2, only analyze the axisymmetric gradient balance of TCs.

Axisymmetric analysis allows for better radial dropsonde data coverage and the gradient balance interpretation is simpler. However, many TCs have asymmetries that make axisymmetric analysis a poor representation of the actual storm structure.

The major challenge of calculating the gradient wind was retrieving the TCBL pressure gradient. Dropsondes and flight level in situ sensors take pressure observations, but the methodology used in this study was not able to optimally incorporate the dropsonde observations. Objective analysis is sensitive to data gaps, so using a realistic horizontal spatial resolution of dropsondes causes the estimated fields to be unconstrained between drops. This leads to local unrealistically large pressure gradient retrievals without sufficient horizontal smoothing. Unfortunately, increasing the horizontal smoothing reduces the retrieved pressure gradient, leading to a bias in the SGW retrieval.

Dropsondes pressure observations have higher errors of  $\sim 1$  hPa (Hock and Franklin 1999) than the flight level in situ pressure observations of  $\sim 0.1$  hPa. There are also small errors in location due to uncertainty in the hydrostatic integration and GPS position. Pressure gradients around  $0.1 - 3.0$  hPa  $\text{km}^{-1}$  must be resolved in the inner core, so high accuracy is required. For these reasons, dropsonde data were eliminated for this pressure gradient analysis. Dropsondes are nonetheless a valuable data source and better ways to incorporate them will be tested in future work.

## **2.2 Hurricane Rita (2005)**

Rita became a tropical storm at 1800 UTC 18 September 2005. Over the next 36 hours Rita moved from east of the Bahamas to just north of Cuba as it intensified to a

category 5 hurricane. The Best Track history of Rita is shown in Figure 2.1 (National Hurricane Center). The Hurricane Rainband and Intensity Change Experiment (RAINEX) field campaign used “figure-four” and concentric flight patterns to sample the TC (Bell et al. 2012b). RAINEX aircraft reconnaissance missions occurred on 19, 21, 22, and 23 September as Rita became an increasing threat to land. Rita’s peak intensity was reached around 0300 UTC 22 September with  $80 \text{ m s}^{-1}$  maximum 1-minute sustained surface winds, and a central pressure of 895 hPa (NHC Tropical Cyclone Report). An eyewall replacement cycle (ERC) occurred on 22-23 September and was captured by RAINEX missions. After the ERC, Rita curved towards the west-northwest and weakened to a category 3 by the time it made landfall in southwest Louisiana on 24 September.

### **2.3 WRF Simulation**

The Weather Research and Forecasting (WRF) model version 3.4.1 was used to simulate Hurricane Rita for 84 hours starting on 18 September 00 UTC and ending on 21 September 12 UTC. The simulation used four nested grids with an 18 km domain spanning  $5400 \times 5400 \text{ km}$  ( $29,160,000 \text{ km}^2$ ), 6 km domain spanning  $1500 \times 1500 \text{ km}$  ( $2,250,000 \text{ km}^2$ ), 2 km domain spanning  $500 \times 500 \text{ km}$  ( $250,000 \text{ km}^2$ ), and 666.7 m domain spanning  $200.67 \times 200.67 \text{ km}$  ( $40,268.45 \text{ km}^2$ ). The three innermost grids followed the 700 hPa vortex. The vertical resolution was 28 sigma levels, unevenly spaced to provide higher resolution in the boundary layer. The physics options used were the Yonsei University (YSU) boundary layer, Dudhia shortwave radiation, Rapid Radiation Transfer Model (RRTM) longwave radiation, and WRF double-moment six-

class microphysics. Kain-Fritsch cumulus parameterization was used on the 18 km domain only. The MM5 similarity scheme was used for the surface layer parameterization with modified drag and enthalpy coefficients for TCs.

The boundary conditions and initial fields were provided by the Global Forecast System (GFS) final analysis, with an added  $10 \text{ m s}^{-1}$  Rankine bogus vortex. Figure 2.2a shows that the intensity for the simulated storm matches up well with the real storm's intensity during the rapid intensification. The primary eyewall began to consolidate by 20 September 18 UTC and was well formed and more axisymmetric by 21 September 06 UTC, as shown in Figure 2.3. Due to a deviating track (Figure 2.2b) and failure to undergo SEF, the simulation was not used beyond 21 September. An analysis of the intensifying primary eyewall was therefore used to estimate instrument errors. An extended simulation with an ERC will be considered for future work.

## **2.4 Instrumentation**

As mentioned in Chapter 1, it is important to estimate the magnitude of the supergradient jet through observations to determine the significance of its role in TC intensification and eyewall formation. There are several different instruments used to gather TCBL observations. Airborne Doppler radar, GPS dropsondes, flight level in situ sensors and Stepped Frequency Microwave Radiometers (SFMR) are used to retrieve the wind and pressure gradient fields from Hurricane Rita. Synthetic observations are used to sample the simulated Rita. First the real observations will be described, followed by the synthetic observations.

### 2.4.1 RAINEX Data

The RAINEX field campaign sent flights into Rita from 19 to 23 September. Observations from the National Oceanic and Atmospheric Administration (NOAA) N42RF WP- 3D (N42) and the Naval Research Laboratory WP-3D (NRL) on 22 September were used in this study. The tracks of the two planes crossed in the northern sector of Rita at 18 UTC as shown in Figure 2.4. All dropsonde and flight level data were quality controlled to remove noise and instrument errors.

Airborne Doppler radar can provide some of the highest resolution wind measurements near the top of the TCBL, so data from Doppler X-band tail radars are used in this analysis (Hildebrand et al. 1996; Jorgensen et al. 1996). The TCBL wind retrieval is similar to that described in Lorsolo et al. (2010) in that it is performed in a “wedge” below the aircraft. Different sizes of this wedge are tested in Chapter 3.1.

Tail radars each have a fore and an aft beam, allowing for dual-Doppler wind retrievals, illustrated in Figure 2.5. The N42 tail radar has pointing angles of  $\pm 19.5^\circ$  and a beamwidth of  $1.9^\circ$ . The along-track resolution is 1.5 km and the range gate is 75 m. Electra Doppler radar (ELDORA) on the NRL has pointing angles of  $\pm 15^\circ$ . The horizontal resolution is higher at 400 m and the range gates are 150 m. At 18 UTC during an ERC the N42 and the NRL crossed paths in the southern (not shown) and northern moat region, giving the best geometry for data synthesis. This “quad-Doppler” analysis (Jorgensen et al. 1996) provides less uncertainty in the resolved winds. The raw observations were processed using a high-threshold automated quality control script in National Center for Atmospheric Research (NCAR) Solo II software to remove airplane motion, false echoes, wind aliasing, and second trip echoes (Bell et al. 2013). An

example of the edited radar observations in Solo II is shown in Fig. 2.6a. The data quality is degraded near the sea surface due to sea spray contamination so this data are removed.

The flight level of the N42 ranged between 1.5 and 2 km altitude, while the NRL was higher between 3 and 4 km during this mission. In situ flight level sensors measure temperature, pressure, and dew point temperature, altitude, and horizontal wind speed and direction. The sampling resolution is 1 second or about 120-130 m along the flight track.

GPS dropsondes can provide near surface kinematic and thermodynamic information in the TCBL, but have their own limitations. The GPS sensor provides the latitude, longitude, and height, from which horizontal winds can be derived. Sensors measure relative humidity, temperature, and pressure with errors less than 5%, 0.2 C and 0.5 hPa, respectively. The vertical sampling rate is  $\sim 7$  m as dropsondes fall at  $12\text{--}15\text{ m s}^{-1}$ . The horizontal sampling rate is much lower (i.e. 1 per 20 km or more) than the flight level observations, and highly variable due to limited dropsonde releases. There is a 0.5 second lag from when the measurement is taken and when the signal is transmitted, causing the estimated pressure retrieval uncertainties to be as high as 1 hPa (Hock and Franklin 1999). The azimuthally averaged horizontal resolution is better, ranging from 1-4 km, as shown in Figure 2.7a along with flight level data. Figure 2.7b shows the azimuthal coverage of dropsondes by all missions on 21 and 22 September. Only the blue dropsondes on 22 September are used in this study. Both N42 and NRL dropsondes were included in parts of the analysis, but some of them failed before they reached the surface.

The center fixes for the real data were found using a cubic spline to fit the centers that maximize the tangential wind at the radius of maximum wind (RMW). A 3 km annulus of radar data is centered on the RMW (Marks et al. 1992; Bell et al. 2012b). When radar data were not available, aircraft center fixes were used. The estimated error of this track is less than 3 km (Bell et al. 2012b).

### **2.4.2 Synthetic Data**

For Chapter 3, synthetic observations are modeled after the real observations and tested to determine the lowest possible error in wind, pressure gradient, and SGW retrievals. Synthetic observations are taken from 20 September 19 UTC during rapid intensification in the primary eyewall. The N42 was simulated to fly in a straight line from the eye to the north at 1.5 km altitude.

The airborne Doppler radar data was created using a program called *AnalyticAircraft* (<https://github.com/mmbell/analyticAircraft>). The simulated flight track is overlain on the modeled dBZ field in Figure 2.8, and is travelling at a constant speed of  $120 \text{ m s}^{-1}$ . The simulated radar is similar to the N42 tail radar, with a wavelength of 3.2 cm, a range gate of 150 m, and pointing angles of  $\pm 19.5^\circ$ . An example of synthetic radar data is shown in Figure 2.6b. Some important simplifications were made for the modeled beam. The beamwidth is infinitesimal, the ocean surface is assumed to be perfectly flat and stationary, and the fore and aft beams have instantaneous sampling time. The synthetic radar data was edited using an automatic quality control script in Solo II. No noise has been added, so any error in the Doppler retrieved wind is due to beam geometry, the specified instrument error, velocity unfolding errors, and the way the data

is edited to remove the surface.

In situ flight level observations were also simulated using a script. The script samples the WRF output along the simulated flight track at every 100 m, calculates the dew point temperature, total wind speed and direction, and outputs to a usable real flight level data format. The flight level is constant at 1.5 km, the same height the synthetic dropsondes are “released” from.

A script was made to simulate GPS dropsondes along the same flight track. The script utilizes a “dropsonde” program that allows each dropsonde to be advected with the wind as it falls and samples the WRF output. From this the total wind speed and direction are calculated, and a dropsonde data file is output in the correct format. Different horizontal resolutions were tested and will be discussed in Chapter 3.1.

SFMR are useful at retrieving surface wind speed that is otherwise difficult to get. SFMR indirectly measures wind speed from the microwave emissivity of the sea surface; but to get the directional components one of several assumptions must be made. In a strong TC the tangential wind is much stronger than the radial wind, so all of the wind speed can be attributed to the tangential component. Alternatively, a constant inflow angle can be assumed at all azimuth and radii. Most likely a more complicated method will be needed where the inflow angle depends on radius, azimuth, TC translational speed, and intensity (Zhang and Uhlhorn 2012). Only the first assumption has been tested so far, using another script. The 10 m u and v components of the wind were used to calculate the total wind speed and direction. Initial tests show that this implementation is not ideal and other methods should be tested for retrieving the u and v components of the wind. Further testing of the SFMR retrievals is deferred for future work.



For axisymmetric wind retrievals and to examine other parts of the storm individually, the AnalyticAircraft XML files were altered to simulate a flight through an additional three radials, east, west and south. The data distribution retrieved at this range is typical for a figure-four flight pattern, which is common for hurricane reconnaissance. Synthetic flights were conducted for six-hour increments from 18 September 12 UTC to 21 September 12 UTC to examine the evolution of the simulated storm, and demonstrate that analysis at 20 September 19 UTC gives representative errors.

## **2.5 SAMURAI**

An improved methodology to retrieve high-resolution low-level TC kinematic and thermodynamic fields uses a new 3D variational analysis technique called SAMURAI (Bell 2010; Bell et al. 2012a). This software program was originally developed to objectively analyze mesoscale axisymmetric features in storm-relative 2D cylindrical space. It now also has the capability of Cartesian or asymmetric analysis in 3D space. It was developed to deal with the problem of estimating the atmospheric state from relatively few actual measurements.

SAMURAI minimizes a variational cost function in observational space to estimate the “true” state of the atmosphere. Cubic B-splines are used as a basis for the atmospheric state representation. A cubic B-spline, a variation of the Bézier curve, is a piecewise polynomial function with three internal knots that has continuous first and second derivatives. Bayesian first principles are applied and it is assumed that the probability distribution of observation and background errors are unbiased and Gaussian. An efficient Galerkin approach is used which sets this program apart from other

variational solvers, such as Gao et al. (2004) and Reasor et al. (2009).

This method is advantageous in several other ways. The use of overlapping cubic B-splines allows for a better fit to observations than a single third-degree polynomial, which has been used in previous studies. The spline interpolation essentially yields similar results to interpolating with higher degree polynomials without the numerical instability. The use of splines also allows for easier application of boundary conditions because the coefficients near the edge of the domain can be set to fulfill desired requirements.

The SAMURAI variational analysis is performed directly in cylindrical coordinates centered on the estimated TC circulation using Doppler radar, SFMR, flight level, and dropsonde observations to take advantage of multiple observations. The variational analysis avoids errors associated with interpolating radar observations to a regular grid. The inversion of the background error covariance matrix is avoided by solving for the incremental form of the cost function. Additional balance or physical constraints, such as conservation of mass, can be applied, but are not used for this study. Another advantage is that observation error specifications can be set for each variable on different instruments.

One disadvantage is that the B-splines are more computationally expensive. Therefore, a control variable state vector is used to speed up the convergence of the minimization. From this vector all physical variables can be derived. The control variable state vector is  $q(x, y, z) = \{\rho u, \rho v, \rho w, T', q', \rho_\alpha'\}^T$  where  $\rho u$  is the mass-weighted u wind component,  $\rho v$  is the mass-weighted v wind component,  $\rho w$  is the mass-weighted w wind component,  $q$  is the water vapor mixing ratio,  $\rho_\alpha$  is the air

density. Prime variables represent perturbations relative to the hydrostatic reference state of Dunion's (2011) moist tropical mean sounding.

A  $4\Delta x$  (4 km) recursive filter is applied in the radial direction and a  $2\Delta z$  (200 m) recursive filter is applied in the vertical direction for the wind retrieval. The purpose of these filters is to define the spatial influence of any single observation and act as diffusive low-pass filters. The filters are useful for filling in data-gaps, but may remove some fine-scale detail. For this study, variation in azimuth can be removed for any given leg by setting the azimuthal component to wavenumber zero. The background error standard deviation was set very high because the prior background state is unknown, causing the spline analysis to be unconstrained where there are data gaps. The data gaps prove to be a challenge in the pressure gradient analysis, as discussed in Chapter 2.1.

The same 4 km radial filter is applied for the pressure gradient retrieval. However, a vertical mean is used because only flight level data at 1.5 km are included. The thermodynamic perturbations are assumed to be the same at each height, by applying a vertical wavenumber zero in SAMURAI. Even though the perturbations are constant with height, the reference state changes with height. Vertical variation in the retrieved pressure field is due to changes in the reference state of water vapor mixing ratio ( $q_v$ ), air density ( $\rho_a$ ), and temperature ( $T$ ). The density weighting ( $1/\rho$ ) of the pressure gradient also changes with height using this method. The main concern of using this method is that enhanced pressure gradients near the surface will not be captured in the analysis. This analysis is not ideal, the pressure gradient field is very difficult to quantify with limited observations. However it is more realistic than previous methods using a cubic polynomial or parametric profile fit to dropsonde observations, as discussed in Chapter

1.2.3. A detailed comparison between the different data fitting techniques is deferred to future work.

### **3 Simulated Primary Eyewall**

#### **3.1 Wind Analysis**

Several different test cases were run to retrieve the low-level winds using the simulated airborne radar, and a combination of other observations, shown in Table 1. The synthetic radar observations of the WRF simulation were analyzed using SAMURAI for the “test” run. Perfect in situ wind observations from the model were also analyzed using SAMURAI for the “truth” run. The outputs were then compared to see how accurate the methodology could be given perfect airborne radar observations. The analyses had no variation in the azimuthal direction in order to determine the optimal width of the data wedge.

The value of adding in situ observations in the variational solution was also tested. Synthetic dropsonde observations were created from the model data and added to the SAMURAI input. Dropsonde spacings of 1, 4, and 8 km each were tested (Table 1 rows 6-8). Flight- level observations were also created from the model data at 1.5 km height, to match the flight altitude of the real data test case (Table 1 row 9).

Figure 3.1a shows the tangential and radial wind from the SAMURAI test using only airborne radar data. There is a tangential wind maximum of  $50 \text{ m s}^{-1}$  at 34 km radius with radial convergence near the surface. The inflow height is generally around 0.75 km, but is lower approaching the eye and highest in the updraft. The “test” field matches well with the “truth” field, as shown in Figure 3.1b, and the difference between

the two is quantified below.

Table 1 shows the results of the different tests of the methodology as root mean square error (RMSE) values between the modeled (truth) and retrieved (test) winds averaged over all heights and from a radius of 10 to 50 km. The rows show the different combinations of observations for retrieving the wind speeds in the V (tangential) and U (radial) directions, and show how much value is added by each observation experiment. For comparison, the RMS values of the wind components are  $38.95 \text{ m s}^{-1}$  for V, and  $3.45 \text{ m s}^{-1}$  for U. The tests show that the radar retrieval alone has an RMSE of  $2.72 \text{ m s}^{-1}$  for V and  $1.46 \text{ m s}^{-1}$  for U (Table 1 row 1) using an azimuthal width of 25 degrees. The RMSE values yield relative errors of 7% for V and 42% for U. Adding flight level in situ data decreased the error to  $2.35 \text{ m s}^{-1}$  and  $1.39 \text{ m s}^{-1}$  respectively. Including dropsonde observations every kilometer was found to improve the V component RMSE to  $2.41 \text{ m s}^{-1}$  and greatly improve the U component, to  $0.96 \text{ m s}^{-1}$  (Table 1 row 6). When all of the types of observations are used the RMSE is improved to  $2.31 \text{ m s}^{-1}$  for V and  $0.93 \text{ m s}^{-1}$  for U (Table 1 row 10).

A paired Student's t-Test was performed for each SAMURAI test to determine if the error reductions were statistically significant. The t-Test paired the mean absolute error (MAE) of the analysis using only radar observations and an azimuthal width of 25 degrees ("control") with the absolute mean error of each test. The MAE change for every test was found to be statistically significant at or above the 99% confidence level compared to the control run. The most notable RMSE changes were found by decreasing the azimuthal width of the analysis wedge (Table 1 rows 1-5). The errors increased as the wedge size decreased, suggesting a trade-off between azimuthal spatial resolution and

wind accuracy.

Adding dropsonde observations to the analysis significantly improved both V and U in all cases. The relative error reduction was greatest for U, suggesting that dropsondes can provide valuable information to help constrain the under-resolved along-track radar-derived winds (Hildebrand et al. 1996). Adding flight level in situ observations to the analysis also reduced the errors, and the greatest error reduction was found using radar, dropsondes, and flight level data. The resulting relative errors were reduced to 6% for V and 26% for U (Table 1 row 10). These results suggest that the technique can produce reasonable wind fields with radar-derived winds alone, but incorporating multiple in situ measurements does add significant value to the analysis.

The radar data is shown to add much of the value to the V and U retrievals (Table 1 row 11). A SAMURAI test was done using only in situ flight level data and dropsonde data every 8 km. The V had a RMSE of  $21.86 \text{ m s}^{-1}$  or 56%, while the U had a RMSE of  $2.52 \text{ m s}^{-1}$  or 73%. This is not surprising because the density of radar observations is much higher than that of flight level and dropsonde observations. The SGW could not be retrieved well without the use of airborne Doppler radar data using this methodology.

To verify that the north leg errors are representative of the other parts of the simulated storm, the error analysis was also done for the south, east, and west legs in the same manner. Only one test run was done for these additional cases. The wind was retrieved using the synthetic radar data, in situ flight level data and dropsondes every 8 km. This combination of observations was chosen because it is the best retrieval while still having realistic horizontal resolutions for this type of mission. Table 2 shows that tangential and radial wind RMSE for the south leg are very similar to the north leg. The

west leg has lower tangential wind RMSE, at  $1.51 \text{ m s}^{-1}$ , and higher radial wind RMSE, at  $4.39 \text{ m s}^{-1}$ . The east leg had lower tangential wind RMSE, at  $1.85 \text{ m s}^{-1}$ , and higher radial wind RMSE, at  $2.52 \text{ m s}^{-1}$ . Overall, it is clear that the tangential wind error is small compared to the magnitude of the tangential wind. The radial wind error appears to be more variable and higher compared to the magnitude of the radial wind, but it is not as critical for the SGW analysis.

Figure 3.2 shows how close to the surface the winds can accurately be estimated using radar winds alone. It appears that the V wind component can be accurately estimated down to 300 m before errors increase, while U can be accurately estimated down to  $\sim 500$  m. The error at the surface is due to the surface echo removal and does not include the effects of residual sea spray contamination. Including flight level data in the analysis reduces the error at 1.5 km altitude. Dropsondes significantly improve U and V near the surface. The vertical error distribution is promising because supergradient jets are expected to be above within 0.2 and 1.5 km of the surface (Kepert 2006b).

### **3.2 Pressure Gradient Analysis**

The pressure gradient is the main source of error in the gradient wind calculation, especially at larger radii. Figure 3.3 shows the SAMURAI output fields for the “truth” (a) and “test” (b) pressure gradients. It is clear that the high gradient near the surface of the “truth” field is being missed by the methodology. The error contribution was tested analytically by calculating the gradient wind for varying pressure gradients (DPDR) and radius (Figure 3.4). The calculated gradient wind gets much larger with increasing radius from center for any given DPDR. At 60 km radius, with a DPDR of  $2 \text{ hPa km}^{-1}$ , the

calculated gradient wind is about  $100 \text{ m s}^{-1}$ . The same DPDR at 20 km radius gives a gradient wind of almost half that speed due to a larger centrifugal force. This analysis only extends from 10 to 50 km radius, but Figure 3.4 shows a large variation over this range for DPDR values greater than  $1 \text{ hPa km}^{-1}$ .

Figure 3.5 shows the gradient wind error as a percentage of the gradient wind with DPDR magnitude and a range of possible DPDR errors. This plot highlights another issue, which effects the gradient wind calculation at smaller DPDR magnitudes and at all radii. If DPDR error is only  $0.1 \text{ hPa km}^{-1}$  the percent error is below 10% for a DPDR magnitude of  $0.5 \text{ hPa km}^{-1}$ , which is typical (Figures 3.3a, b). However a DPDR error on the same order as the pressure gradient magnitude yields a 40% error in the gradient wind.

The actual pressure gradient errors were calculated in the same way as the wind error analysis. Table 2 shows DPDR errors as RMSE, using only in situ flight level data compared to the “truth” field for each quadrant. Although the DPDR fields show significant differences (Figure 3.3a, b), the magnitudes match up reasonably well, except at the surface near 22 km radius. Typical RMSE values are near  $0.01 \text{ hPa km}^{-1}$ .

### **3.3 Supergradient Wind Analysis**

At the analyzed time the simulated storm was undergoing rapid intensification as the primary eyewall consolidated. The north leg has an interesting double rainband feature, while the south leg has less convection. The west leg is the cross-section with the deepest convection, while the east leg has the broadest region of convection (see Figure 2.8). Subgradient flow is expected at the surface, and possibly radially outside the



RMW. Ideally, supergradient jets are expected at the top of the boundary layer (500-1000 m), a few km radially inward of the RMW. A deceleration in radial inflow is expected below the jet, indicating convergence and upward motion.

Using the retrieved wind and pressure gradient fields, Equation 7 was used to calculate the agradient wind. Figure 3.6a shows the resulting agradient wind in the “truth” field for the simulated storm. The expected subgradient flow is observed ( $-6 \text{ m s}^{-1}$ ) at most of the lower levels. There are three supergradient maxima at 13, 30, and 40 km radii, all centered on altitudes of 500 m. The magnitudes are around  $6$  to  $8 \text{ m s}^{-1}$ . The “test” agradient wind is shown in Figure 3.7b, with much higher magnitudes, especially at the surface. No subgradient flow is observed at the surface and there are three maxima in SGW around  $12$  to  $14 \text{ m s}^{-1}$ . The reason for high SGW magnitudes near the surface is that the pressure gradient methodology under-resolves the low-level pressure gradients, causing a low bias in the calculated gradient wind. The wind retrieval was also shown to be worst at the surface.

Although the results for SGW are not good in the north leg, they are helpful in quantifying the magnitude of the SGW uncertainty attributed to observations. The north leg at 19 UTC 20 September was selected for the double rainband feature that appears morphologically similar to a double eyewall. However, the feature is not dynamically the same as a double eyewall, which may explain why the SGW field does not look as expected. In fact, an analysis done only an hour before, at 18 UTC 20 September (not shown) has a SGW pattern that is more expected. There is a single, well-defined RMW in the north leg at this time, and a supergradient get just radially inward of it.

An error analysis (Table 2, last column) shows that the RMSE of SGW is  $5.8 \text{ m s}^{-1}$

<sup>1</sup> for the north leg. The RMSE is slightly lower for the other legs, ranging from 5.0 to 4.6  $\text{m s}^{-1}$ . If the true magnitude of SGW is only around 5  $\text{m s}^{-1}$  as in some numerical models and the “truth” fields, then this analysis suggests that observations will not be able to resolve the SGW well.

### 3.4 Axisymmetric Analysis

To test the axisymmetric retrievals, settings in the SAMURAI analysis file were changed to include observations from all azimuths. The scripts were altered to retrieve synthetic observations from the simulated storm at the north, south, east, and west radials. This pattern is similar to the “figure-four” patterns often flown by reconnaissance aircraft in hurricanes.

The wind retrieval shown in Figure 3.7b uses synthetic radar data, dropsondes every 8 km, and flight level data. The 8 km horizontal resolution of dropsondes was chosen to represent a realistic, though ambitious flight mission. The previous wind analysis shows that this wind retrieval is not very sensitive to different dropsonde horizontal resolutions.

The axisymmetric wind analysis looks similar to the north leg analysis, but the RMW is smaller by almost 10 km and  $V_{\text{max}}$  is 5  $\text{m s}^{-1}$  lower. The “truth” axisymmetric wind (Fig. 3.7a) looks nearly identical to the retrieved wind (Fig. 3.7b), except near the surface where the retrieved wind does not decrease as much. The error analysis for the axisymmetric storm at 19 UTC 20 September gives a V RMSE value of 1.55  $\text{m s}^{-1}$  and a

U RMSE value of  $0.90 \text{ m s}^{-1}$ . The axisymmetric V retrieval is better than most of the single leg analyses, although more model times should be tested to strengthen the statistics.

The pressure gradient retrieval shown in Figure 3.8b used flight level in situ data from the four radials. The DPDR magnitude ranges from  $0.1$  to  $0.5 \text{ hPa km}^{-1}$ , similar to the north leg retrieval. Clearly the strongest pressure gradient ( $0.7 \text{ hPa km}^{-1}$ ) is at the surface near  $24 \text{ km}$  radius (Figure 3.8a), and this is not captured when including only flight level data. The error analysis gives a low RMSE value of  $0.01 \text{ hPa km}^{-1}$ , similar to the north leg pressure gradient RMSE. The RMSE does not appear to capture the pointwise error in the pressure gradient, which is an order of magnitude higher.

The “truth” SGW (Figure 3.9a) is weaker than that of the north leg, but qualitatively similar. The “test” SGW, shown in Figure 3.9b, has the same issue as the north leg SGW analysis. The surface shows high SGW of  $14 \text{ m s}^{-1}$  due to difficulties in the pressure gradient retrieval. There is no well-defined jet just inside the RMW. The error analysis gives a RMSE of  $4.5 \text{ m s}^{-1}$ , lower than all of the individual legs. Of course, this type of analysis is not as useful for highly asymmetric storms and at 19 UTC 20 September, the simulated Rita was still asymmetric. The axisymmetric analysis can be expected to improve later in the WRF run, when the eyewall is more axisymmetric and the SGW is expected to be stronger.

The pressure gradient was tested further and retrieved using both in situ flight level and dropsonde data together. The analysis was similar, but included dropsondes with increased instrument errors to reduce their weight in the analysis. The instrument errors must be increased to account for uncertainties in pressure and location. The

resulting SGW is shown in Figure 3.9c. The SGW analysis is worse than using flight level in situ data alone (Figure 3.9b), with unrealistically high magnitudes. While it is generally preferred to use all available observations, this methodology cannot incorporate the dropsonde data well. Testing different ways to change the methodology and include dropsonde data is deferred to future work.

## **4 Real Primary and Secondary Eyewall**

### **4.1 Wind Analysis**

The real data case using the new methodology was performed with observations from two RAINEX flights into Hurricane Rita at 18 UTC 22 September 2005. Three SAMURAI test cases were run. The first used only radar data from N42 and the second test included radar, dropsonde, and flight level data from N42. To further validate the methodology, the third test compares these retrievals to a “quad-Doppler” analysis that includes ELDORA observations and dropsondes from the same time and area. Figure 4.1 shows the comparison of the wind fields. There is a primary eyewall at 20 km and a secondary eyewall at 42 km radius. The radius-height cross-section in the storm’s northern quadrant reveals a stronger primary eyewall and weaker secondary eyewall, but with stronger inflow near the secondary eyewall. These results are consistent with a developing secondary eyewall at this time. The maximum tangential wind speed is approaching  $70 \text{ m s}^{-1}$  at 20 km radius and  $55 \text{ m s}^{-1}$  around 42 km radius. A maximum of  $12 \text{ m s}^{-1}$  inflow is below the primary wind maximum, with sharp deceleration towards the inner edge. There is another inflow maximum below and radially outward of the secondary wind maximum of  $20 \text{ m s}^{-1}$ , with some deceleration near the inner edge of the

secondary wind maximum. The quad-Doppler analysis, which is considered a skillful way to retrieve TC winds (Bell et al. 2012b ) shows good agreement with the analysis using only NOAA observations.

#### **4.2 Pressure Gradient Analysis**

The pressure gradient retrieved from N42 in situ flight level data is shown in Figure 4.2. The same methodology was applied as in the simulated eyewall analysis. The magnitude of the retrieved pressure gradient is much higher at this time, ranging from -1 to +3 hPa km<sup>-1</sup>. Higher pressure gradients are expected because Rita has intensified to a category 4 hurricane at this time. There is a marked increase in the pressure gradient near 18 km radius, just inside of the primary eyewall where the highest gradients would be expected. At outer radii, near the developing secondary wind maximum, the pressure gradients are much lower and there is only a small increase near 42 km radius. The pressure gradient becomes negative in the eye, meaning the pressure is increasing at the TC center. Strongly negative pressure gradients are unrealistic in a TC and are a result of unconstrained analysis where data is sparse. A single leg of flight level data does not appear to be enough for the pressure gradient retrieval using this methodology.

#### **4.3 Supergradient Wind Analysis**

The SGW is expected to peak just radially inward of the primary and secondary wind maxima at the top of the boundary layer. Figure 4.3 shows the resulting SGW from the north leg. There is a supergradient jet just radially outside of the primary wind max at

about 22 km radius, from the surface to 300 m height with a peak value of  $20 \text{ m s}^{-1}$  (29%) supergradient. There is a second supergradient jet concurrent with the secondary wind maximum, at 41 km radius and 700 m height. The magnitude is slightly lower, at  $18 \text{ m s}^{-1}$  (30%) supergradient. There is subgradient wind at the surface, except near the two tangential wind maxima. The wind is less supergradient ( $4 \text{ m s}^{-1}$ ) in the moat region, but should probably be subgradient. From 10 to 12 km radius, there is unrealistic SGW resulting from the nearly flat pressure gradient there and limited amount of data.

#### **4.4 Axisymmetric Analysis**

The axisymmetric tangential wind analysis consisting of both the south and north legs (Figure 4.4) reveals a similar structure to the north leg wind analysis alone. There is a primary radius of maximum winds at 18-20 km radius that extends from 300 m to 1.5 km. There is a decrease in tangential winds near 30 km radius in the “moat” and a secondary wind maximum at 40 km radius. There is strong inflow beneath the primary wind maximum that rapidly decelerates at the inner edge, indicating convergence (Figure 4.4). There is strong radial inflow beneath and just outside the secondary wind maximum, which also decelerates slightly as it approaches the maximum. A weak region of outflow is located above and just inside the secondary wind maximum.

The axisymmetric pressure gradient analysis (Figure 4.5) does not look like the north leg field. It is more slowly changing throughout with values ranging from 0.6 to  $2 \text{ hPa km}^{-1}$ . This is less extreme than the north leg due to the averaging of the north and south legs leading to a more reasonable axisymmetric SGW analysis.

The pressure gradient was also retrieved using both in situ flight level and dropsonde data. The resulting SGW is shown in Figure 4.6a. It looks similar to the SGW field using only flight level data (Figure 4.6b), but has higher magnitudes and the analysis is unconstrained where there is a data gap from 35 to 38 km radius (seen in Figure 2.7a). As a result there are unrealistic SGW magnitudes at these radii and the shape of the secondary supergradient jet is lost. The comparison between Figures 4.6a and b further demonstrates how sensitive the methodology is to observation resolutions and how difficult it is to get the high-resolution pressure gradient and SGW fields for a real TC. The in situ only analysis is believed to more accurately capture the agradient winds than that including dropsondes.

The axisymmetric analysis of the SGW field overlaid on the wind field is shown in Figure 4.7 (black lines). There is a supergradient jet at 17 km radius and 300 m height, just inside of the primary wind maximum and near the top of the inflow. The secondary supergradient jet is at 40 km radius and 700 m height, inside the secondary wind maximum. The higher altitude of the secondary jet is consistent with the height of the boundary layer increasing with radius (Ooyama 1982; Zhang et al. 2011). The magnitudes are  $22 \text{ m s}^{-1}$  (29%) for the primary supergradient jet and  $16 \text{ m s}^{-1}$  (25%) for the secondary jet. The SGW pattern is similar to the expected structure, but the magnitudes are slightly higher than previous studies, which suggest winds were 10-25% supergradient (Kepert and Wang 2001).

Figure 4.8 shows a comparison between the retrieved flight level in situ pressure observations (north and south legs), the axisymmetric SAMURAI pressure analysis, and the axisymmetric cubic polynomial pressure with radius. The R-value for the cubic

polynomial is high (0.98) meaning the pressure fit is very good. However, some local gradients in pressure are not captured at all. For example, at 12 and 25 km radius (Figure 4.8) the cubic B-spline is a better fit than the cubic polynomial, but both fits underestimate the pressure gradient around 20 km radius. There is a visible difference between the pressure profiles of the north and south legs, indicating that the axisymmetric analysis may be smoothing out important variations in pressure gradient. After 55 km radius, the cubic polynomial begins to drop off, while the SAMURAI analysis follows the real observations as they continue to increase. From this quick comparison, it appears the spline method is superior.

## **5. Conclusion and Discussion**

There are several theories for the initiation of secondary eyewalls in intense TCs. Although many ERCs have been observed by satellite (Hawkins et al. 2006), relatively few of them have been directly observed by aircraft. Some notable examples include Hurricane Anita in 1977 (Willoughby 1979), Hurricane David in 1979 (Willoughby et al. 1982), Hurricane Gilbert in 1988 (Black and Willoughby 1992; Dodge et al. 1999), and Hurricane Rita in 2005 (Bell et al, 2012; Didlake and Houze 2011).

A new methodology for retrieving the SGW from observations in the TCBL has been presented. The TCBL is a difficult place to get high-resolution wind and pressure gradient fields from observations. This study uses a variational analysis technique called SAMURAI to combine multiple types of observations.

First, the primary eyewall of Rita (2005) was simulated with the WRF model. The model fields were then synthetically observed by flying a simulated aircraft equipped



with in situ sensors, Doppler radar and dropwindsondes. The retrieved fields from the synthetic observations were then compared to the model or “truth” fields. From the differences between the two fields, observational errors for the wind, pressure gradient, and SGW were estimated. Next the real Hurricane Rita’s primary and secondary eyewall were analyzed to determine the magnitude of the retrieved SGW. Although the magnitude of SGWs in the real storm was greater, as expected for a more intense TC, both the simulated and real storm retrievals were found to have SGWs that were 21-29% of the maximum tangential wind.

### **5.1 Interpretation of Results**

The methodology was shown to retrieve both tangential and radial wind fields well from one quadrant of the TC. The RMSEs are on the order of 6% for tangential wind and 26% for the radial wind, when radar, dropsondes, and in situ flight level data are incorporated. The axisymmetric wind retrieval was slightly better than the north leg retrieval, with lower RMSE values when compared to the “truth” field. Radar data were shown to be a crucial part of the wind retrieval because of the large spatial coverage.

The pressure gradient analysis was more challenging. The in situ flight level observations were critical to the analysis, so this type of study may have large errors if flight level is above 2 km altitude. The method used for retrieving the pressure gradient caused some high-gradient areas to be missed near the surface. A strength of this methodology is fitting pressure observations to overlapping cubic B-splines, which allows for a more complex gradient wind profile. Single cubic polynomial fits used in previous studies show very good pressure fits, but give an unrealistic quadratic gradient

wind (Bell and Montgomery 2008, Sanger et al. 2014). The Willoughby parametric profile similarly causes the gradient wind to drop off too quickly at outer radii, making it difficult to apply to secondary eyewall scenarios (Willoughby et al. 2006).

The SGW results qualitatively match up well with previous axisymmetric studies that used Rita observations from the same period. Didlake and Houze (2011) calculated gradient balance residuals (GBR) using a cubic polynomial fit at 500 m altitude. Positive GBR correspond to SGWs and negative GBR correspond to subgradient winds. They found a narrow region of positive GBR values just inside of the primary eyewall and a wide region of positive GBR values near the secondary eyewall (their Figure 6). There were negative GBR values in the moat region where this study retrieved weak SGW. Bell et al. (2012b) showed that the radial inflow decelerated sharply just inside of both eyewalls at 100 m altitude (their Figure 10a) indicating the convergence associated with supergradient jets.

The SGW analysis for the simulated primary eyewall showed that for the weak simulated TC ( $V_{\max}$  around  $50 \text{ m s}^{-1}$ ) the SGW is  $4$  to  $6 \text{ m s}^{-1}$ . With a SGW RMSE of  $5 \text{ m s}^{-1}$  (a 100% error), the supergradient jet cannot be well quantified by observations. The synthetic observations retrieved higher SGW of  $14$  to  $16 \text{ m s}^{-1}$ , but the higher magnitudes are caused by under-resolved pressure gradients using the current methodology.

The real primary eyewall SGW magnitudes were found to be up to  $20 \text{ m s}^{-1}$  (29%) for the north leg and  $22 \text{ m s}^{-1}$  (29%) for the axisymmetric storm. The real secondary eyewall SGW magnitudes were up to  $18 \text{ m s}^{-1}$  (26%) for the north leg and  $16 \text{ m s}^{-1}$  (21%) for the axisymmetric storm. The uncertainty in these magnitudes can be deduced using Figures 3.5 and 3.6. Since the gradient wind is around  $50 \text{ m s}^{-1}$  and approximate DPDR

errors are known, it can be estimated that the error in gradient wind is 10%, or  $\sim 5 \text{ m s}^{-1}$ . Including the  $2 \text{ m s}^{-1}$  error from the retrieved wind the highest expected error is  $\sim 7 \text{ m s}^{-1}$ . This is only true in the worst-case scenario where the different sources of error are additive. A more likely typical error is  $\sim 5 \text{ m s}^{-1}$ , which is consistent with the error estimated from the WRF simulation. Using this error, the possible spread of the SGW in the real primary eyewall is 23% to 36%. For the secondary eyewall the SGW is estimated to be 17% to 32%. There are still a lot of uncertainties, but this is a good first step towards quantifying the magnitude of SGWs in the TCBL.

The analysis supports the idea that supergradient jets are significant features associated with both primary and secondary eyewalls. The significance of these jets adds to the evidence that unbalanced boundary layer dynamics may play an important role in TC intensification and SEF. However, determining the dominant mechanisms for SEF are well beyond the scope of this study. More work must be done using observations and numerical models to determine the dominant physical processes at play.

## **5.2 Future Work**

The SAMURAI analysis was found to be sensitive to filter length, data sampling, and errors in retrieved pressure. Although it would be ideal to have more accurate observations closer to the surface, it is not realistic at present. It is considered dangerous for aircraft to fly well into the TCBL in the inner core of intense TCs. Unmanned drones have the potential to sample the TCBL, but are currently too expensive. Cheaper dropsondes may be the answer to retrieving a better pressure gradient field because more

of them could be used. If the data density is high, then averaging can be used to reduce the error, assuming the pressure sensors are not worse.

One way this study can be improved is by testing different horizontal recursive filters. A radial filter of  $4\Delta x$  (4 km) was applied to reduce the low amplitude fluctuations and smooth regions where data is sparse. This filter makes physical sense because the analysis can only resolve features that are  $>5$  km due to the 1 km resolution. The analysis, however, has 1 km resolution in the radial direction and the azimuthal resolution depends on the radius. The analysis is done in a wedge so that the resolution is much higher near the eye than at outer radii. With the current filter it is a concern that unresolved scales may be affecting the results and higher radial filters should be considered. Higher filters can significantly reduce the wind and pressure gradients however, potentially leading to an overestimate of the SGW.

Future work will focus on analyzing the evolution of the SGW over different times of the simulation. The magnitude of the “truth” axisymmetric SGW becomes stronger on 21 September, when the primary eyewall is stronger and more axisymmetric. It would also be preferable to extend the WRF simulation to examine Hurricane Rita on 22 September during SEF. This would give a better comparison between the model and the real data in the context of SEF and it will be interesting to see the magnitudes of SGW in the secondary eyewall from the simulated storm.

The next step includes additional error analysis. Errors in the circulation center estimates will be quantified because they could be significant. Two types of errors must be tested: transverse and radial. The transverse center errors are perpendicular with respect to flight track and cause a change in the partitioning of the wind into U and V

components. The radial center errors are parallel with respect to the flight track and only cause errors due to displacement. Both types of errors could be an issue in the retrieved tangential wind and the calculated gradient wind and depends on the RMW. The error due to the use of streamlines, instead of trajectories, and the neglect of the radial wind in gradient balance will be investigated. The modeled radar beam will be improved and noise will be added to make errors more realistic.

## 6. References

- Abarca, S. F., and M. T. Montgomery, 2013: Essential Dynamics of Secondary Eyewall Formation. *J. Atmos. Sci.*, **70**, 3216-3230.
- Bell, M. M., and M. T. Montgomery, 2008: Observed Structure, Evolution, and Potential Intensity of Category 5 Hurricane Isabel (2003) from 12 to 14 September. *Mon. Wea. Rev.*, **136**, 2023-2046.
- Bell, M. M., M. T. Montgomery, K. A. Emanuel, 2012: Air–Sea Enthalpy and Momentum Exchange at Major Hurricane Wind Speeds Observed during CBLAST. *J. Atmos. Sci.*, **69**, 3197–3222.
- Bell, M. M., Montgomery, M. T., and Lee, W. C., 2012: An Axisymmetric View of Concentric Eyewall Evolution in Hurricane Rita (2005). *J. Atmos. Sci.*, **69** 2414-2432.
- Black, M. L., H. E. Willoughby, 1992: The Concentric Eyewall Cycle of Hurricane Gilbert. *Mon. Wea. Rev.*, **120**, 947–957.
- Brill, K. F., 2014: Revisiting an Old Concept: The Gradient Wind\*. *Mon. Wea. Rev.*, **142**, 1460–1471.
- Didlake, A. C. and Houze, R. A., 2011: Kinematics of the Secondary Eyewall Observed in Hurricane Rita (2005). *J. Atmos. Sci.*, **68**, 1620-1636.
- Dodge, P. R., W. Burpee, and F. D. Marks, 1999: The kinematic structure of a hurricane with sea level pressure less than 900 mb. *Mon. Wea. Rev.*, **127**, 987–1004.
- Foster, R. C., 2009: Boundary-layer Similarity Under an Axisymmetric, Gradient Wind Vortex. *Boundary-layer Meteorology*, **131**, 321-344.
- Gao, J., M. Xue, K. Brewster, and K. K. Droegemeier, 2004: A three-dimensional

- variational data analysis method with recursive filter for Doppler radars. *J. Atmos. Oceanic Technol.*, **21**, 457–469.
- Hawkins, J. D., M. Helveston, T. F. Lee, F. J. Turk, K. Richardson, C. Sampson, J. Kent, and R. Wade, 2006: Tropical cyclone multiple eyewall characteristics. Preprints, 27th Conf. on Hurricane and Tropical Meteorology, Monterey, CA, Amer. Meteor. Soc., 6B.1. [Available online at [http://ams.confex.com/ams/27Hurricanes/techprogram/paper\\_108864.htm](http://ams.confex.com/ams/27Hurricanes/techprogram/paper_108864.htm).]
- Holton, J. R., and G. J. Hakim, 2013: *An Introduction to Dynamic Meteorology*. Academic press, pp.
- Huang, Y. H., Montgomery, M. T., and C.C. Wu, 2012: Concentric Eyewall Formation in Typhoon Sinlaku (2008). Part II: Axisymmetric Dynamical Processes. *J. Atmos. Sci.*, **69**, 662-674.
- Hildebrand, Peter H., and Coauthors, 1996: The ELDORA/ASTRAIA Airborne Doppler Weather Radar: High-Resolution Observations from TOGA COARE. *Bull. Amer. Meteor. Soc.*, **77**, 213–232.
- Jorgensen, D. P., Matejka, T., and J. DuGranrut, 1996: Multi-beam techniques for deriving wind fields from airborne Doppler radars. *Meteorology and Atmospheric Physics*, **59**, 83-104.
- Kepert, J., 2006: Observed Boundary Layer Wind Structure and Balance in the Hurricane Core. Part I: Hurricane Georges. *J. Atmos. Sci.*, **63**, 2169-2193.
- Kepert, J., 2006: Observed Boundary Layer Wind Structure and Balance in the Hurricane Core. Part II: Hurricane Mitch. *J. Atmos. Sci.*, **63**, 2194-2211.

- Kepert, J., 2013: How Does the Boundary Layer Contribute to Eyewall Replacement Cycles in Axisymmetric Tropical Cyclones? *J. Atmos. Sci.*, **70**, 2808-2830.
- Kepert, J., and Y. Wang, 2001: The dynamics of boundary layer jets within the tropical cyclone core. Part II: Nonlinear enhancement. *J. Atmos. Sci.*, **58**, 2485-2501.
- Lorsolo, S., J. A. Zhang, F. Marks, and J. Gamache, 2010: Estimation and Mapping of Hurricane Turbulent Energy Using Airborne Doppler Measurements. *Mon. Wea. Rev.*, **138**, 3656-3670.
- Menelaou, K., Yau, M. K., and Y. Martinez, 2014: Some aspects of the problem of secondary eyewall formation in idealized three-dimensional nonlinear simulations. *Journal of Advances in Modeling Earth Systems*.
- Ooyama, K. V., 1982: Conceptual evolution of the theory and modeling of the tropical cyclone. *J. Meteor. Soc. Japan*, **60**, 369-380.
- Reasor, P. D., M. D. Eastin, and J. F. Gamache, 2009: Rapidly Intensifying Hurricane Guillermo (1997). Part I: Low-wavenumber Structure and Evolution. *Mon. Wea. Rev.*, **137**, 603-631.
- Rozoff, C. M., D. S. Nolan, J. P. Kossin, F. Zhang, and J. Fang, 2012: The Roles of an Expanding Wind Field and Inertial Stability in Tropical Cyclone Secondary Eyewall Formation. *J. Atmos. Sci.*, **69**, 2621-2643.
- Sanger, N. T., M. T. Montgomery, R. K. Smith, and M. M. Bell, 2014: An Observational Study of Tropical Cyclone Spinup in Supertyphoon Jangmi (2008) from 24 to 27 September. *Mon. Wea. Rev.*, **142**, 3-28.
- Sitkowski, M., and G. M. Barnes, 2009: Low-level Thermodynamic, Kinematic, and Reflectivity Fields of Hurricane Guillermo (1997) During Rapid Intensification.



- Mon. Wea. Rev.*, **137**, 645–663.
- Smith, R. K., M. T. Montgomery, and N. Van Sang, 2009: Tropical Cyclone Spin-up Revisited. *Quarterly J. Roy. Meteor. Soc.*, **135**, 1321–1335.
- Smith, R. K. and S. Vogl, 2008: A Simple Model of the Hurricane Boundary Layer Revisited. *Quarterly J. Roy. Meteor. Soc.*, **134**, 337–351.
- Williams, G. J., R. K. Taft, B. D. McNoldy, and W. H. Schubert, 2013: Shock-like Structures in the Tropical Cyclone Boundary Layer. *Journal of Advances in Modeling Earth Systems*, **5**, 338–353.
- Willoughby, H. E., 1979: Excitation of spiral bands in hurricanes by interaction between the symmetric mean vortex and a shearing environmental steering current. *J. Atmos. Sci.*, **36**, 1226–1235.
- Willoughby, H. E., 1990: Gradient Balance in Tropical Cyclones. *J. Atmos. Sci.*, **47**, 265–274.
- Willoughby, H. E., Clos, J. A., and M.G. Shoreibah, 1982: Concentric Eye Walls, Secondary Wind Maxima, and the Evolution of the Hurricane Vortex. *J Atmos. Sci.*, **39**, 395–411.
- Willoughby, H. E., Darling, R. W. R., & Rahn, M. E., 2006: Parametric Representation of the Primary Hurricane Vortex. Part II: A New Family of Sectionally Continuous Profiles. *Mon. Wea. Rev.*, **134**, 1102–1120.
- Wu, C. C., Huang, Y. H., and G. Y. Lien, 2012: Concentric Eyewall Formation in Typhoon Sinlaku (2008). Part I: Assimilation of T-PARC Data Based on the Ensemble Kalman Filter (EnKF). *Mon. Wea. Rev.*, **140**, 506–527.

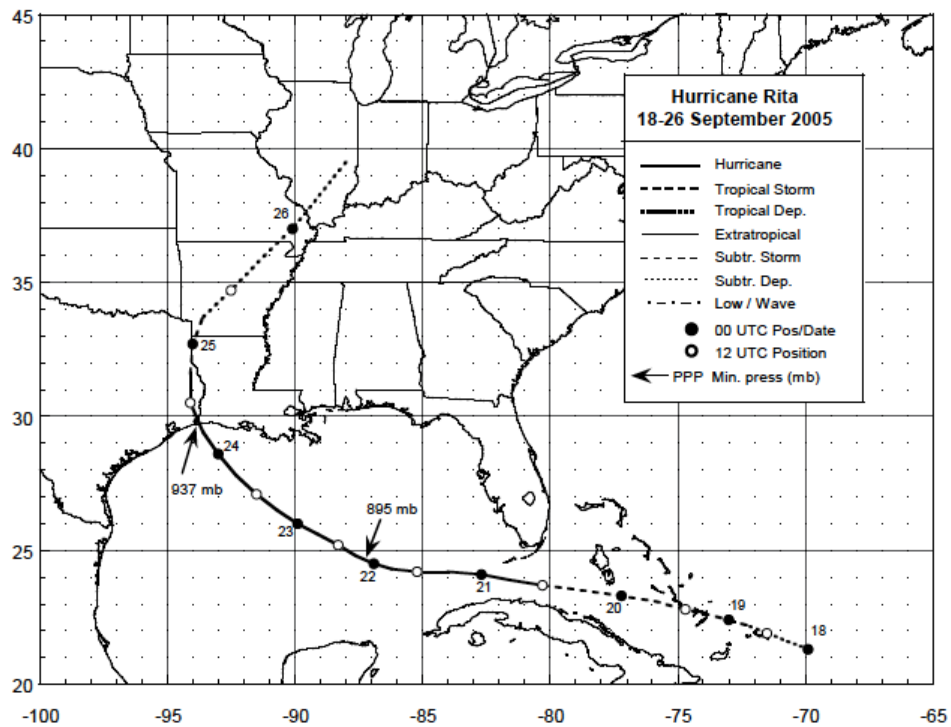
Zhang, J. A., R. F. Rogers, D. S. Nolan, and F. D. Marks, 2011: On the Characteristic Height Scales of the Hurricane Boundary Layer. *Mon. Wea. Rev.*, **139**, 2523-2535.

Table 1 The tangential and radial wind retrieval error analysis given as root mean square error (RMSE) in  $\text{m s}^{-1}$  as last 2 columns. The first 5 columns show the swath width of data taken to get Doppler velocity from radar, where “x” means the variable used in that “test” run. The 6<sup>th</sup> column shows if synthetic radar data were included, columns 7-9 show the horizontal dropsonde resolution, the 10<sup>th</sup> column shows if the flight level data was included. Each row is a different SAMURAI analysis run.

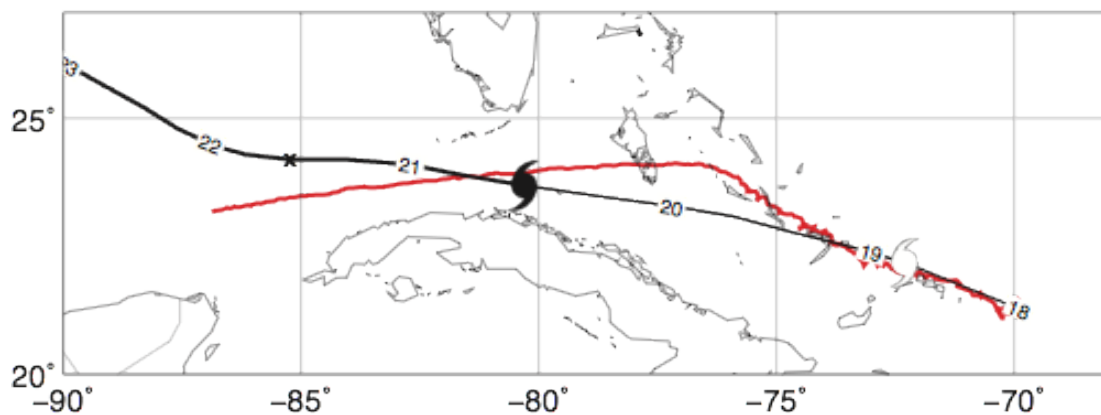
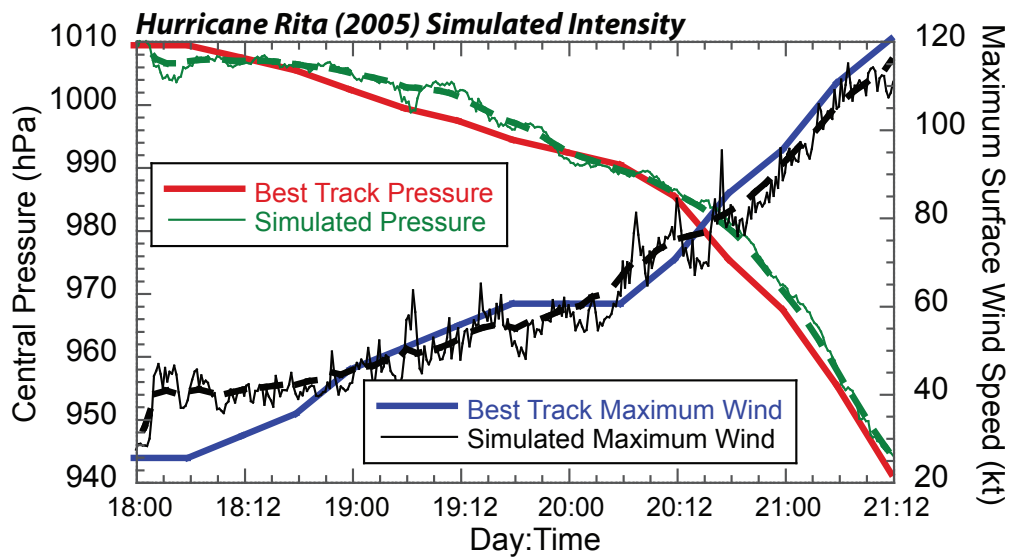
Dtheta (degrees)					Radar	Dropsondes (km)			Flight level	North Leg Error	
5	10	15	20	25	Synthetic	1	4	8	1.5 km	RMSE V	RMSE U
				x	x					2.72	1.46
			x		x					4.31	1.74
		x			x					8.14	2.31
	x				x					12.37	3.37
x					x					18.42	5.48
				x	x	x				2.41	0.96
				x	x		x			2.34	0.93
				x	x			x		2.40	1.10
				x	x				x	2.35	1.39
				x	x	x			x	2.31	0.93
								x	x	21.86	2.52

Table 2 RMSE between “test” and “truth” SAMURAI fields for the axisymmetric run, and the north, south, west, and east leg runs. Column 2 is tangential wind, column 3 is radial wind, column 4 is pressure gradient, and column 5 is SGW.

Leg	RMSE			
	V ( $\text{m s}^{-1}$ )	U ( $\text{m s}^{-1}$ )	DPDR ( $\text{hPa km}^{-1}$ )	SGW ( $\text{m s}^{-1}$ )
Axisymmetric	1.55	0.90	0.0097	4.47
N	2.55	0.54	0.0120	5.80
S	2.40	0.61	0.0106	5.02
W	1.51	4.39	0.0126	4.79
E	1.85	2.52	0.0099	4.59



**Figure 2.1. The National Hurricane Center best-track positions for Hurricane Rita from 18 to 26 September, 2005.**



**Figure 2.2** The WRF simulation intensity compared to the best track intensity data for Hurricane Rita over the 84 hours simulation period (a). The track of the WRF simulated Rita (b).

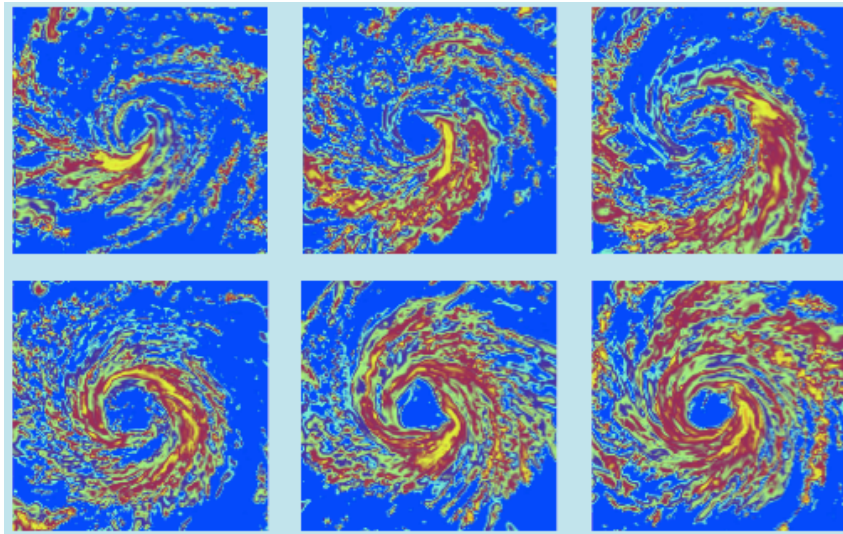


**Figure 2.3** Evolution of the dBZ field in the WRF simulation in 6-hour intervals from 20 September 00 UTC to 21 September 06 UTC.

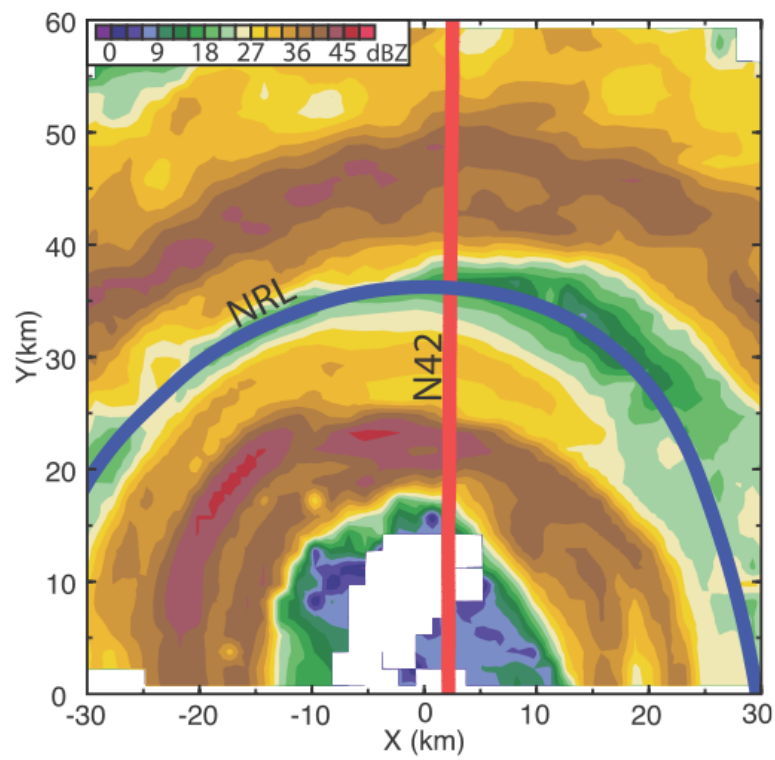


**Figure 2.4** The tracks of the N42 and NRL aircraft at approximately 18 UTC 22 September in the northern part of Rita, overlain on radar reflectivity (from Bell et al. 2012b).

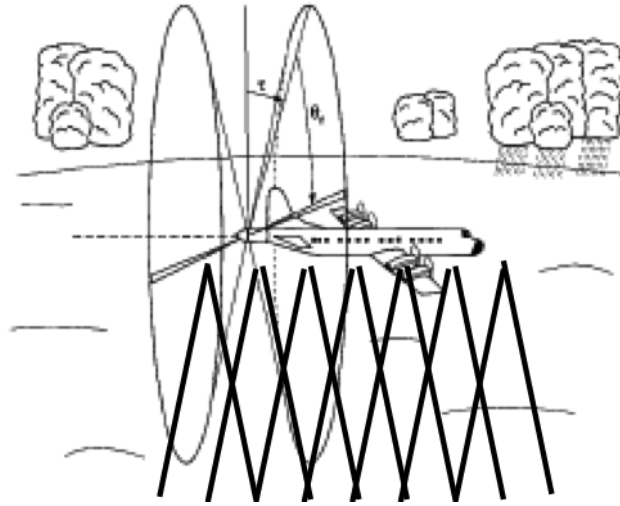


**Figure 2.5** A schematic demonstrating the Dual Doppler wind retrieval from the fore and aft beams of an airborne Doppler tail radar.

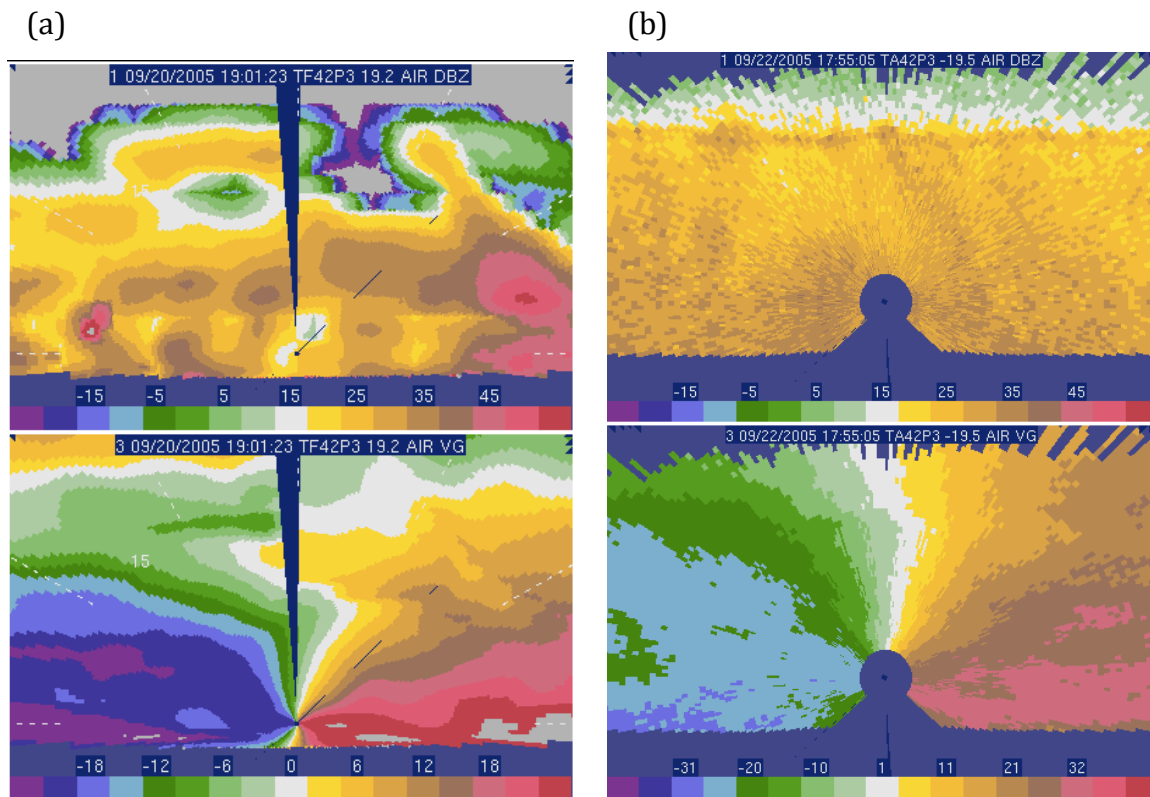
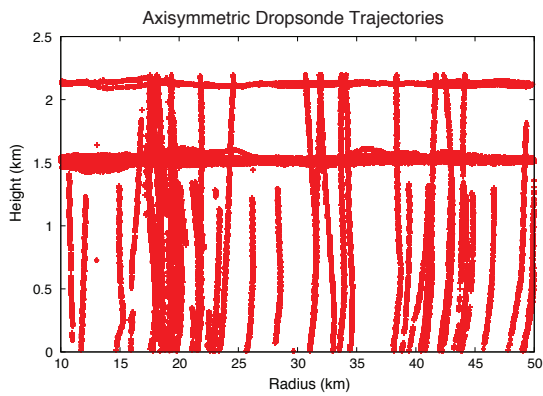


**Figure 2.6** Real (a) and synthetic (b) edited radar data in NCAR Solo II software. The dBZ field (top) and Doppler velocity (bottom) are shown in a radius height cross-section. The central dot is the location of the aircraft.

(a)



(b)

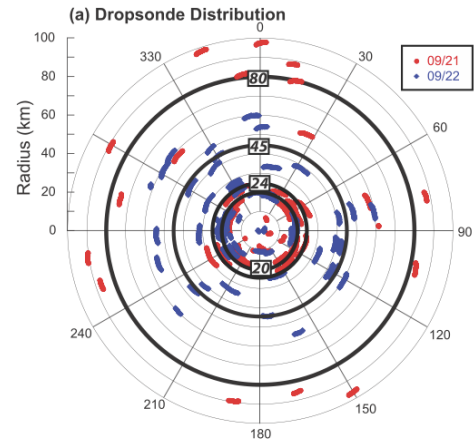


**Figure 2.7 (a) The azimuthally average radial location of dropsondes and in situ flight level observations used from RAINEX. There are data gaps from 35 to 38 km and inward of 10 km. (b) Dropsondes released during missions on 21 (red) and 22 (blue) Sep (from Bell et al. 2012b). The blue lines show dropsondes used in this study.**

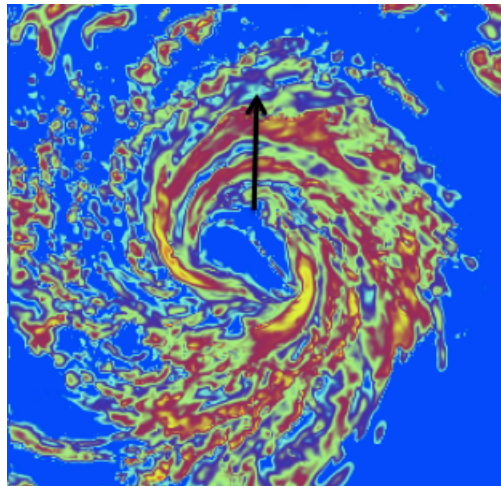


**Figure 2.8 DBZ field during 19 UTC on 20 September with simulated flight track for north leg (black arrow).**



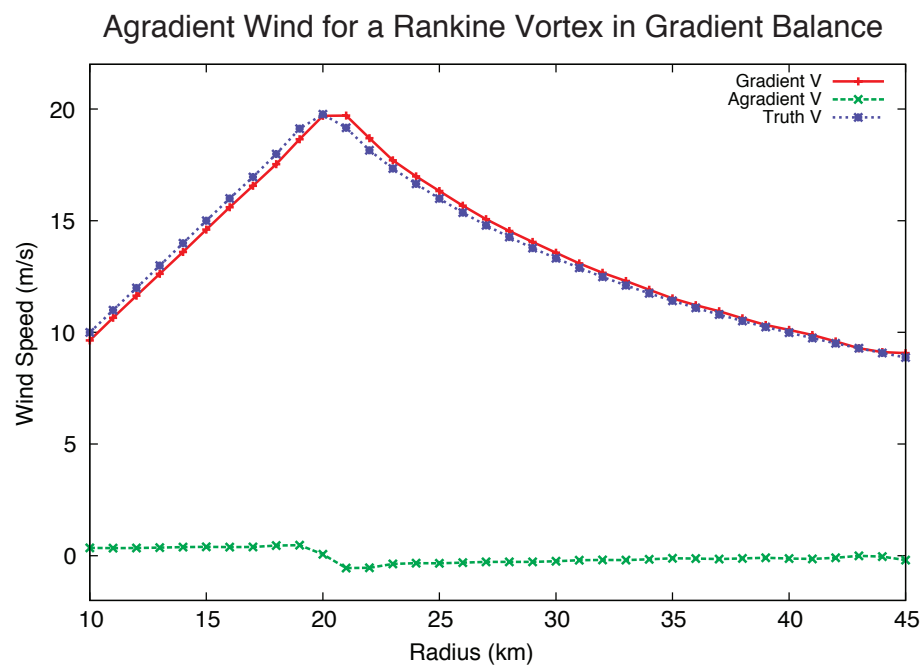


**Figure 2.9** The agradient wind retrieval for a Rankine vortex in gradient balance.

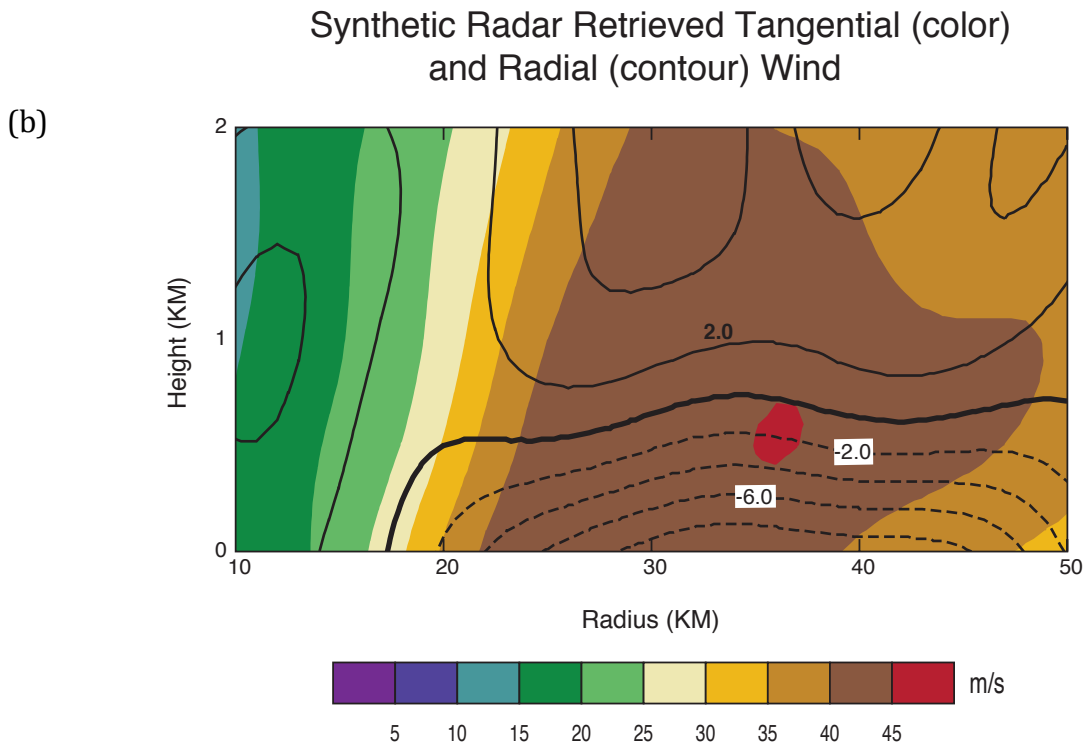
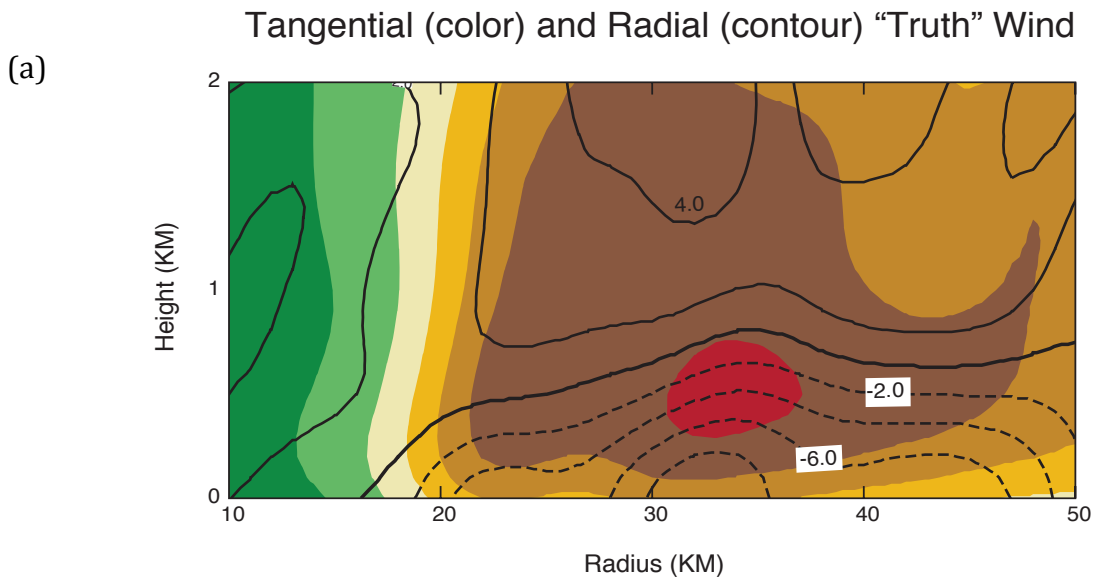


**Figure 3.1** The tangential (color) and radial (black lines) “truth” wind field from SAMURAI (a) as a radius-height cross-section. The bold black line indicates where radial wind is  $0 \text{ m s}^{-1}$ , dashed lines are inflow and solid lines are outflow. The retrieved wind field (b) uses only synthetic radar data in SAMURAI from the north leg at 19 UTC.

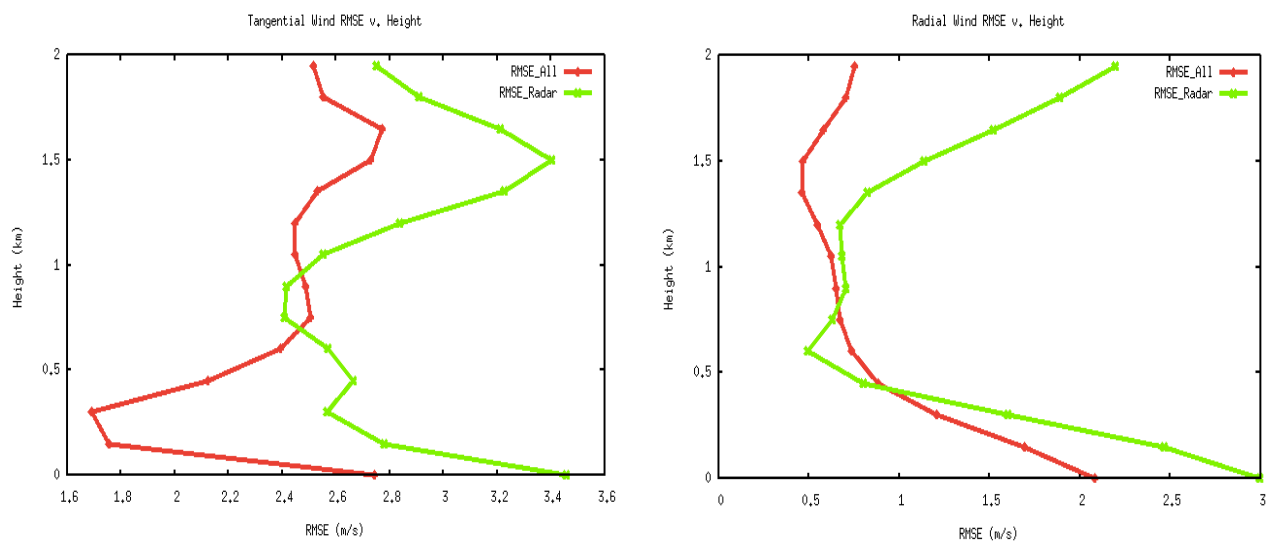


**Figure 3.2 RMSE plotted with height for V (a) and U (b). The green lines show the RMSE for retrievals using only radar data. Red lines show the RMSE for retrievals using radar, dropsondes, and in situ flight level observations. Note that x-axes are different ranges and intervals.**

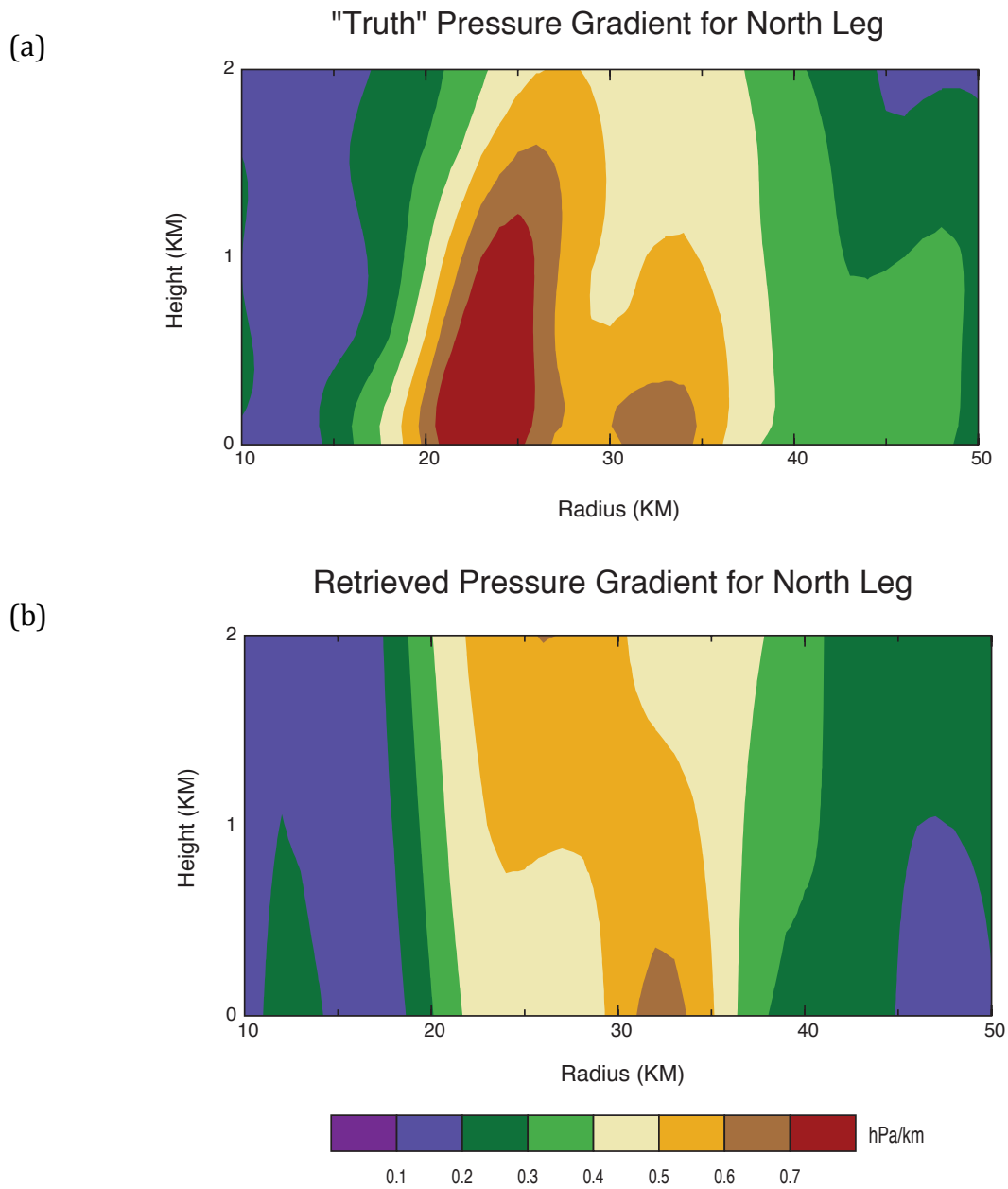


**Figure 3.3 SAMURAI output for the "truth" pressure gradient of the north leg (a). Test SAMURAI output for the retrieved pressure gradient (b) using in situ flight level data.**

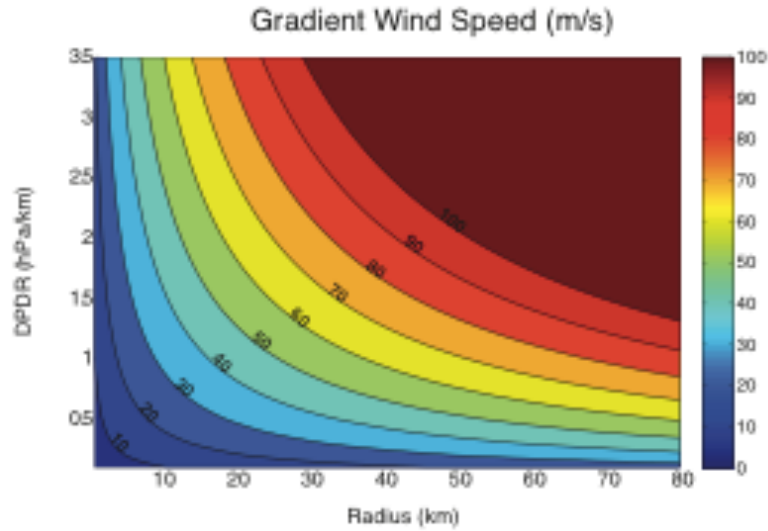


Figure 3.5 Analytic gradient wind speed error (%) as a function of pressure gradient and pressure gradient error ( $\text{hPa km}^{-1}$ ).

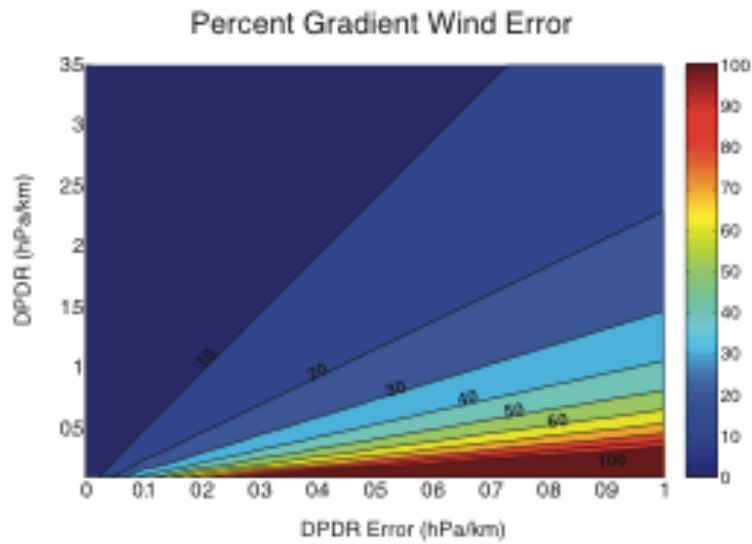
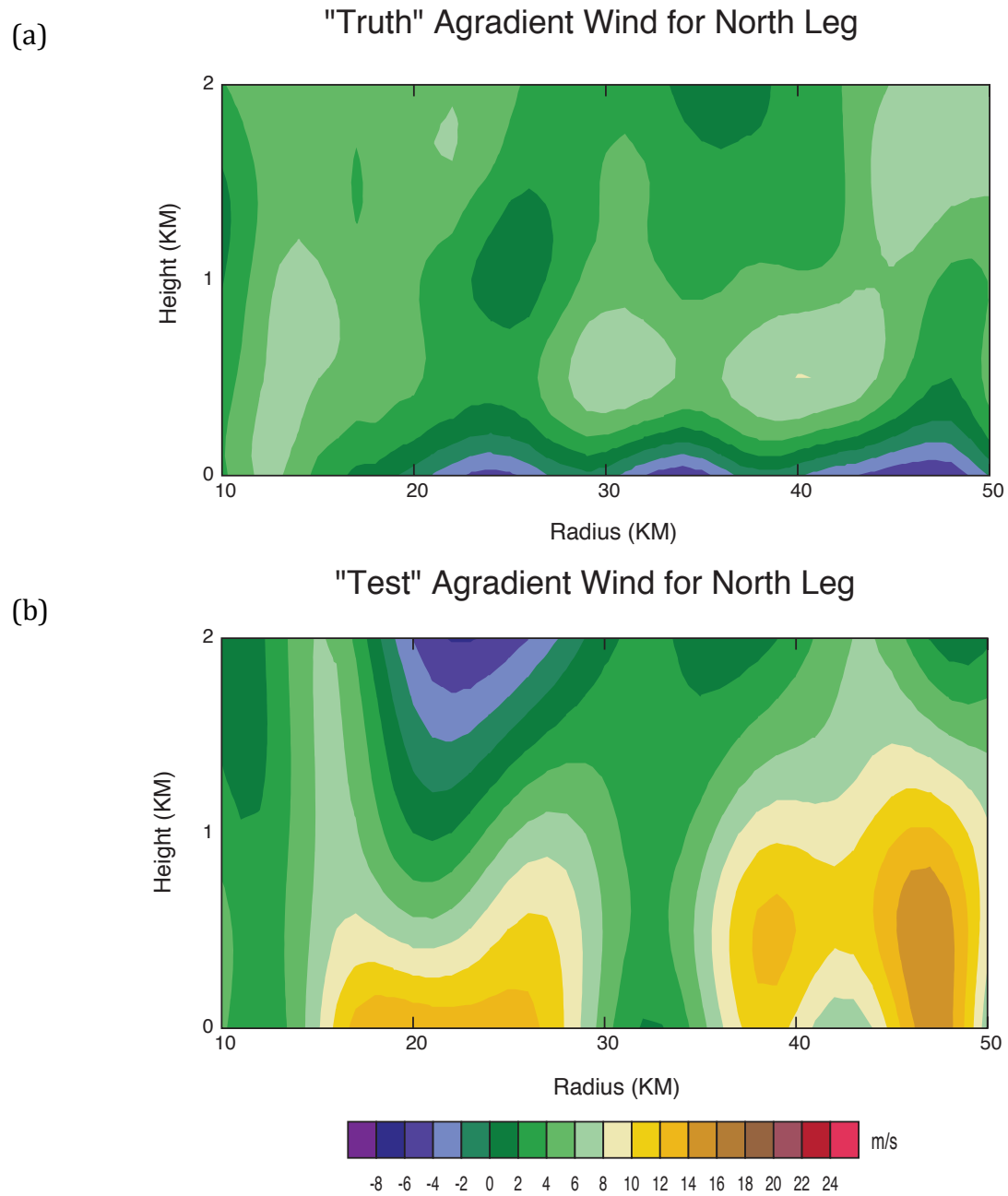
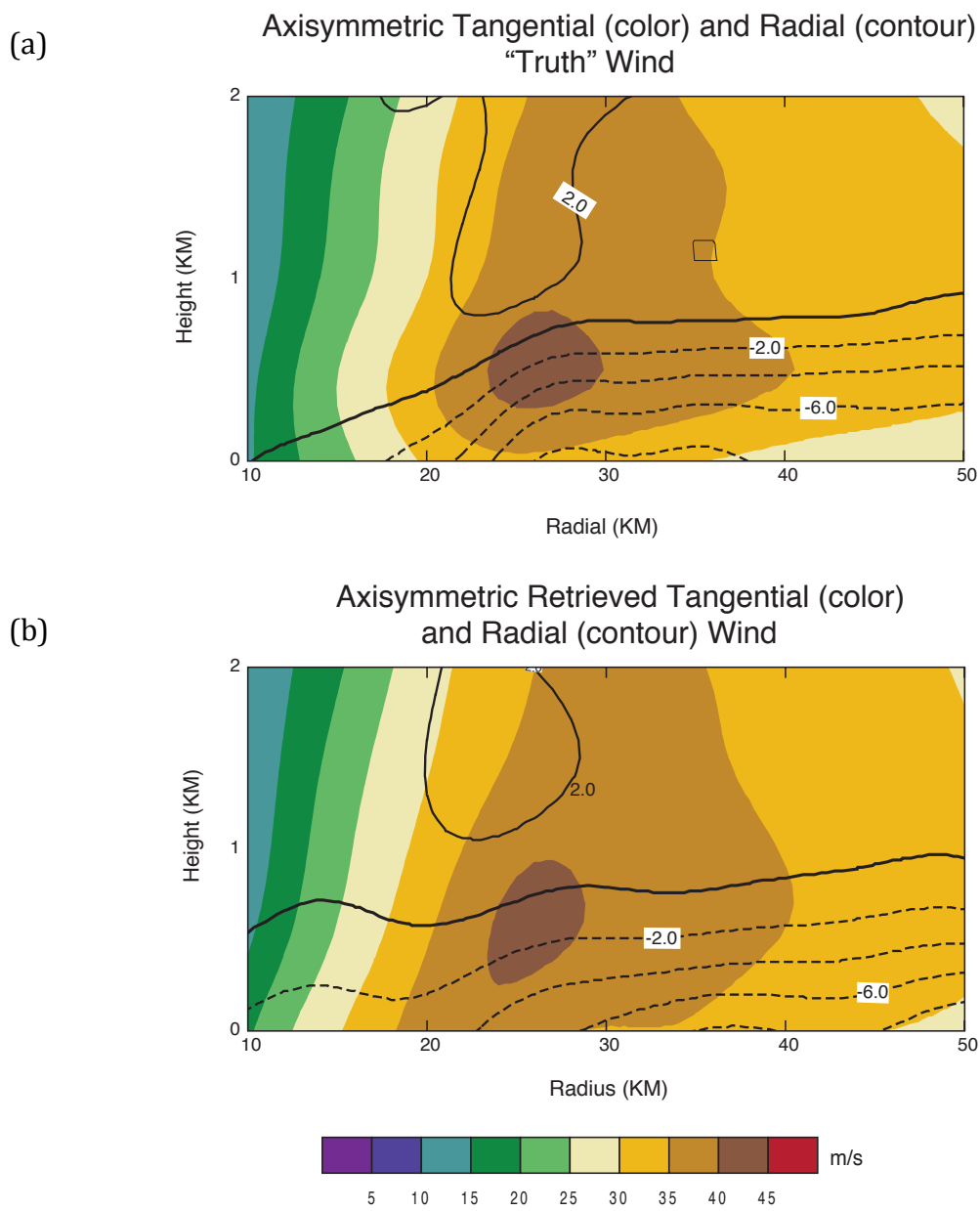


Figure 3.4 Analytic gradient wind speed as a function of radius ( $\text{km}$ ) and radial pressure gradient ( $\text{hPa km}^{-1}$ ). The gradient wind speed is capped at  $100 \text{ m s}^{-1}$  for clarity.



**Figure 3.6 SAMURAI output for the “truth” (a) and "test" (b) SGW field of the north leg at 19 UTC.**



**Figure 3.7** Similar to Figure 3.1. Axisymmetric "truth" (a) and "test" (b) wind fields from SAMURAI.

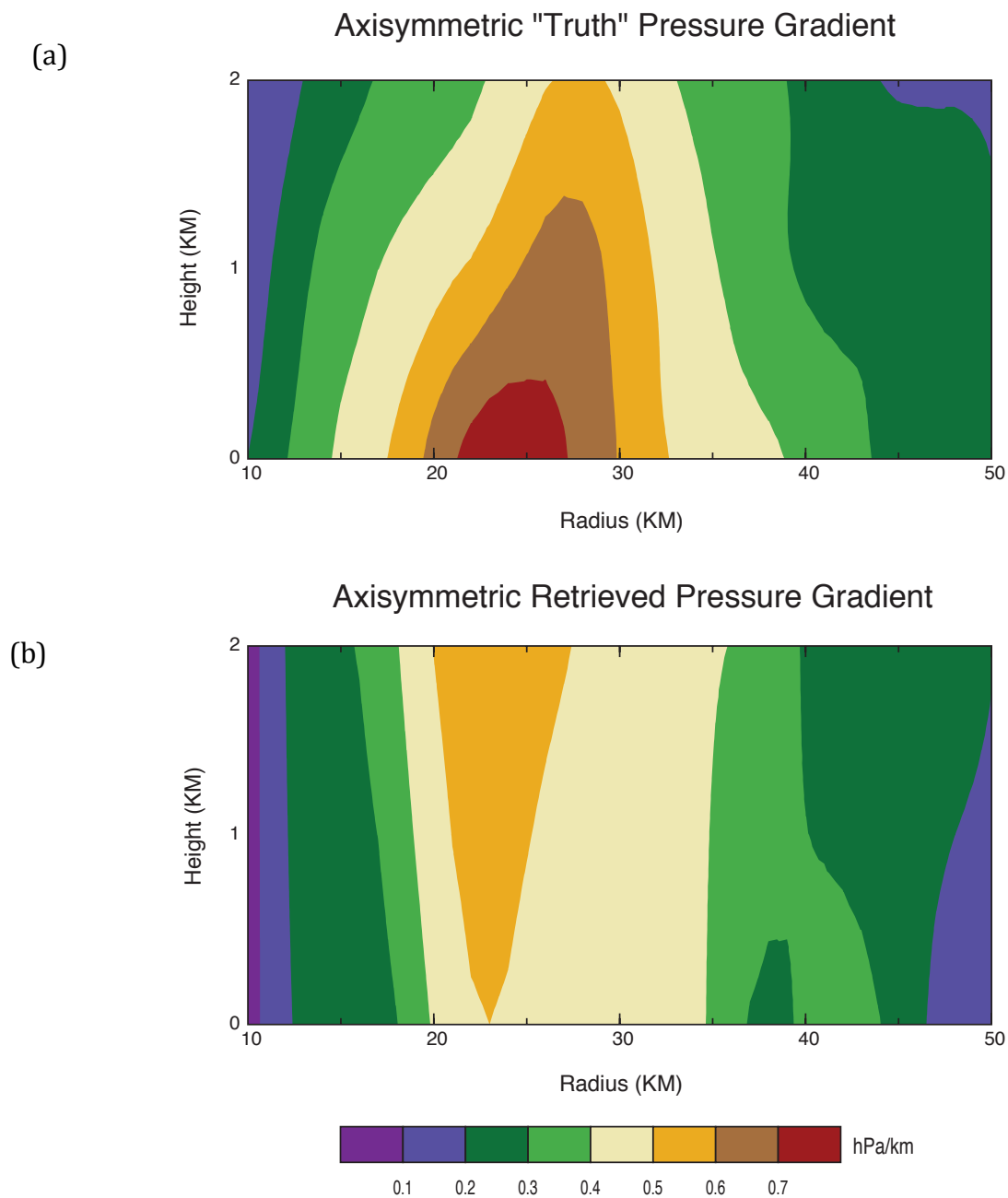


**Figure 3.8** Similar to Figure 3.3. Axisymmetric “truth” (a) and “test” (b) pressure gradient field at 19 UTC.



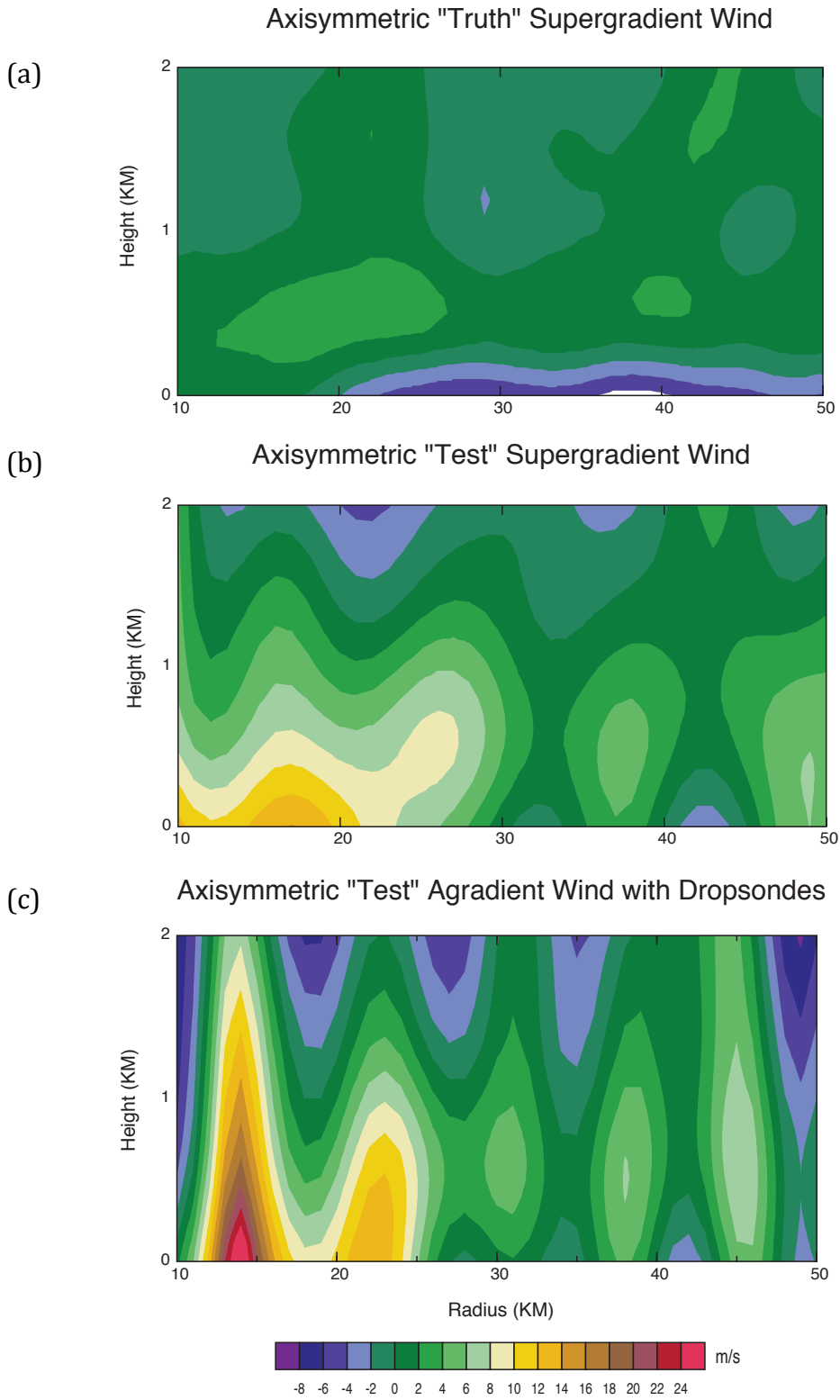


**Figure 3.9** Similar to Figure 3.6. Axisymmetric “truth” (a) and “test” (b) SGW field from SAMURAI output. The “test” SGW using both flight level and dropsonde data (c) has been included for comparison.

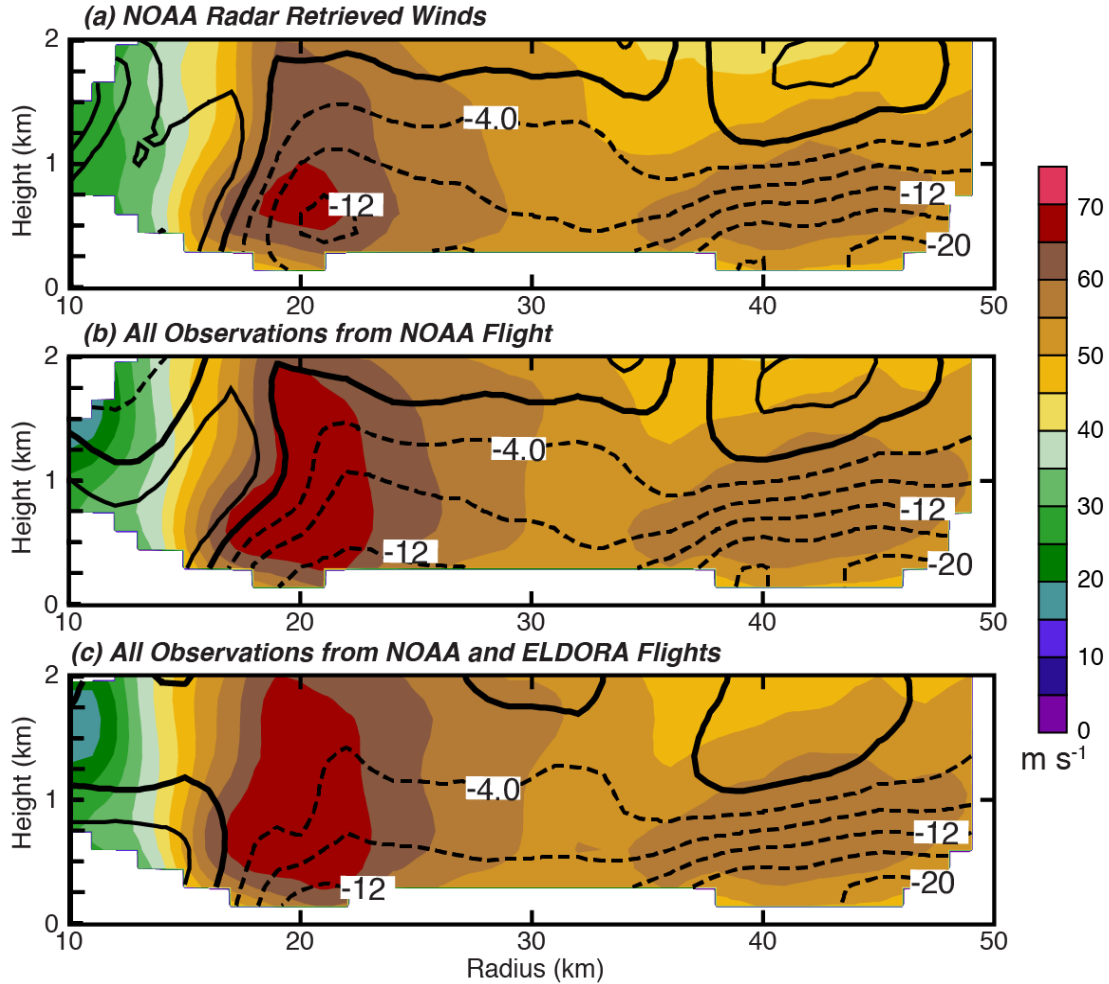


**Figure 4.1** Wind fields from north leg SAMURAI tests using RAINEX observations at 18 UTC 22 September. Tangential wind (color) and radial wind (black lines) were retrieved using only the N42 radar (a), the N42 radar, in situ flight level, and dropsondes (b), and quad-Doppler analysis (c) including ELDORA radar data. The bold black line indicates where radial wind is  $0 \text{ m s}^{-1}$ , dashed lines are inflow and solid lines are outflow.

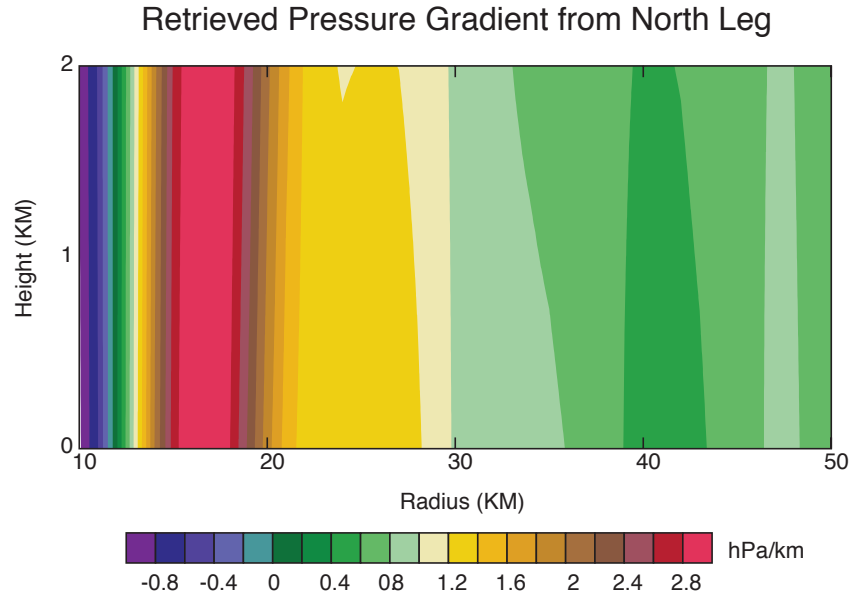


**Figure 4.2** Radius-height cross section of retrieved pressure gradient ( $\text{hPa km}^{-1}$ ) for the real storm from the north leg.

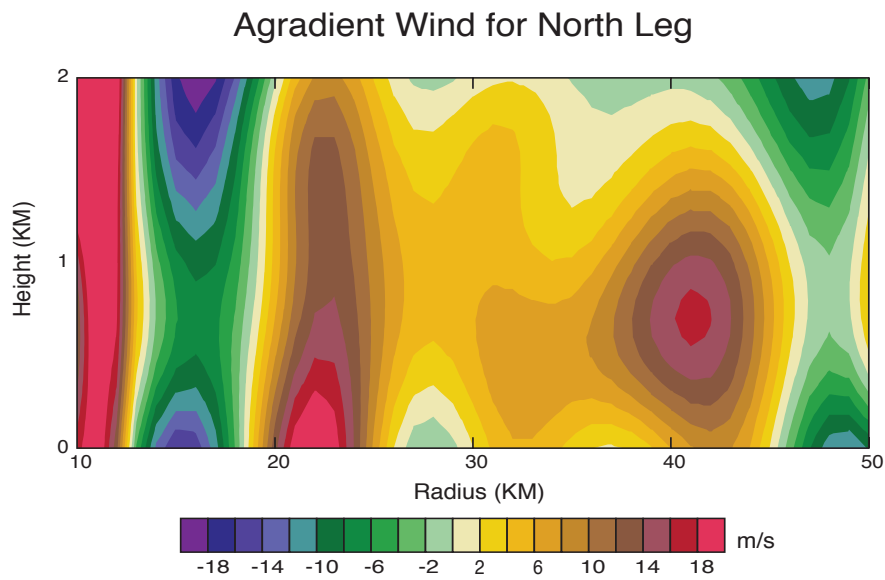


**Figure 4.3** Radius-height cross section of retrieved agradient wind ( $\text{m s}^{-1}$ ) for the real storm north leg.

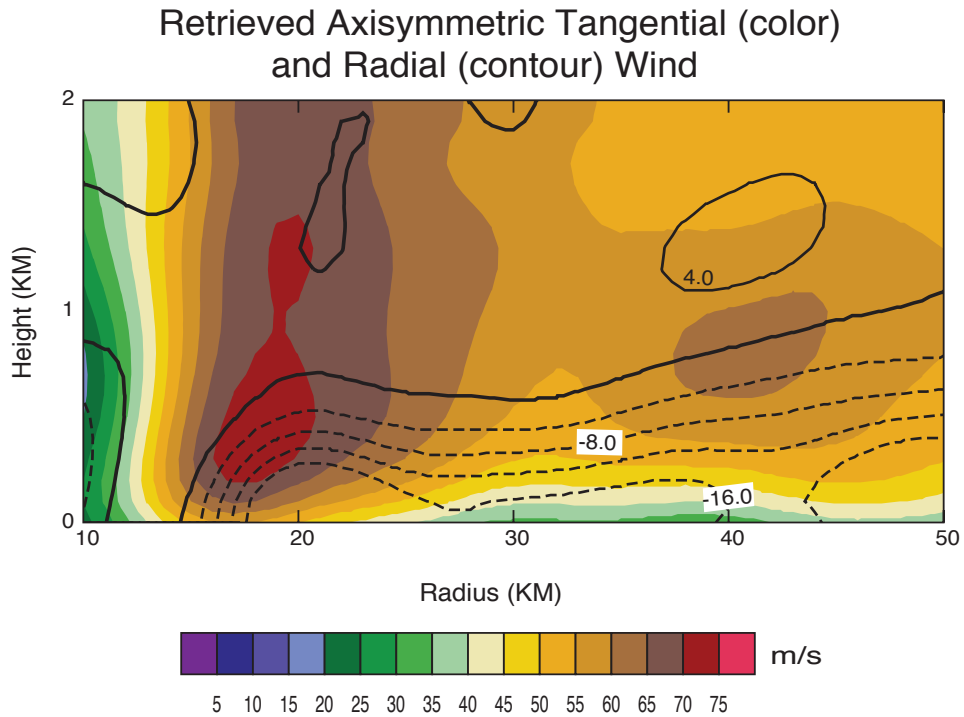


**Figure 4.4** Axisymmetric retrieved tangential (color) and radial (contours) winds, from the SAMURAI test using radar, in situ flight level, and dropsonde data from the N42 and NRL aircraft. The bold black line indicates where radial wind is  $0 \text{ m s}^{-1}$ , dashed lines are inflow and solid lines are outflow.

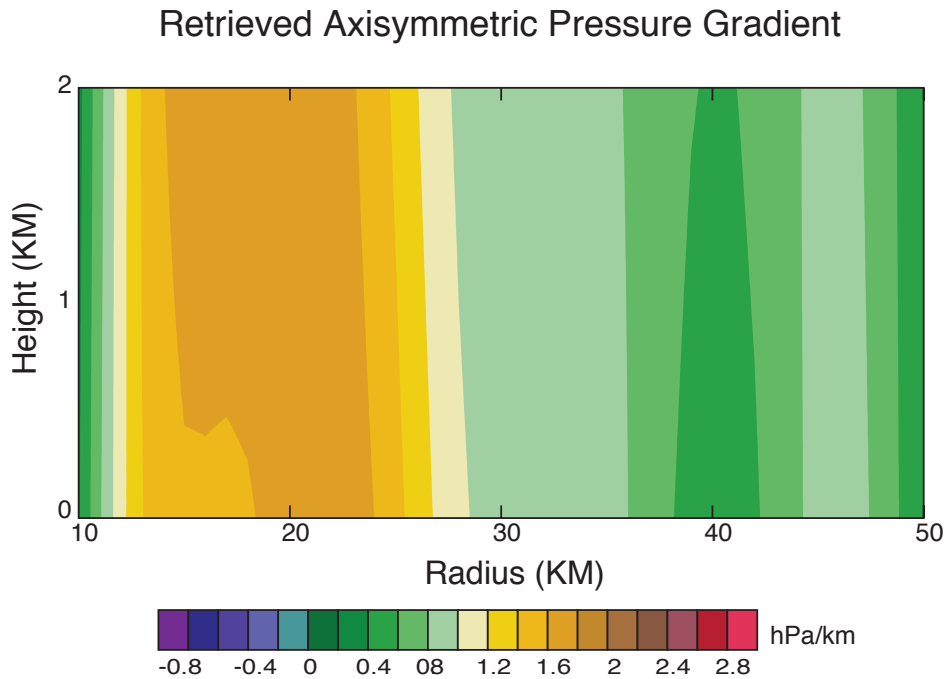
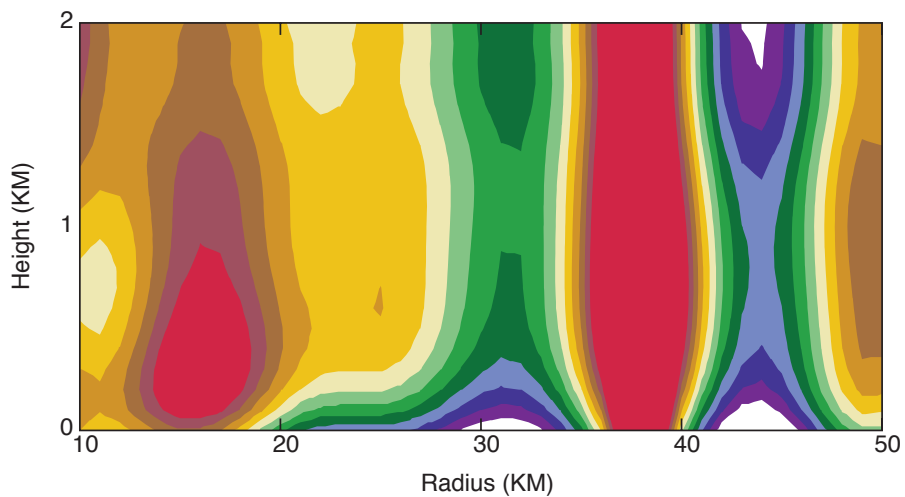


**Figure 4.5** Retrieved axisymmetric pressure gradient ( $\text{hPa km}^{-1}$ ) from N42 in situ flight level observations from the south and north legs.

(a)

### Axisymmetric Agradiant Wind with Dropsonde Data



(b)

### Axisymmetric Agradiant Wind without Dropsonde Data

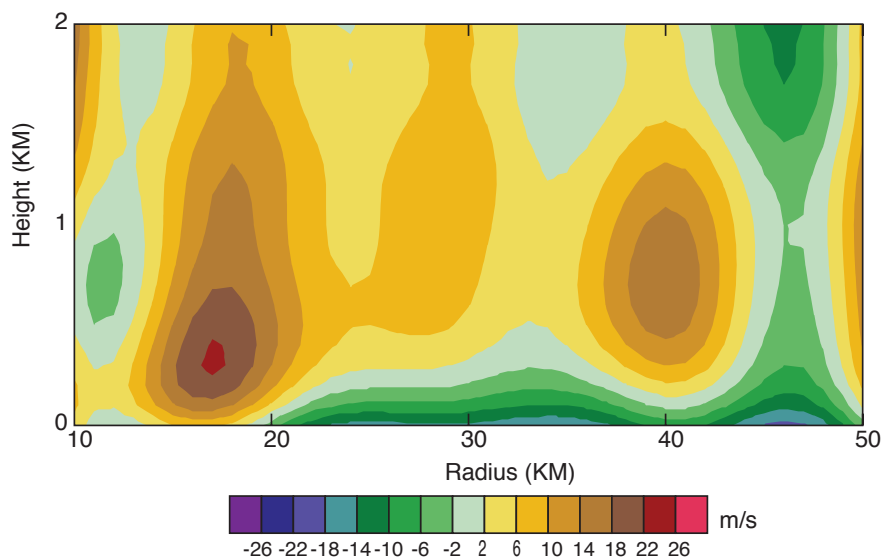


**Figure 4.6 Axisymmetric SGW from 18 UTC 22 September. Pressure gradients were retrieved using flight level in situ and dropsonde data (a) and flight level in situ data only (b).**

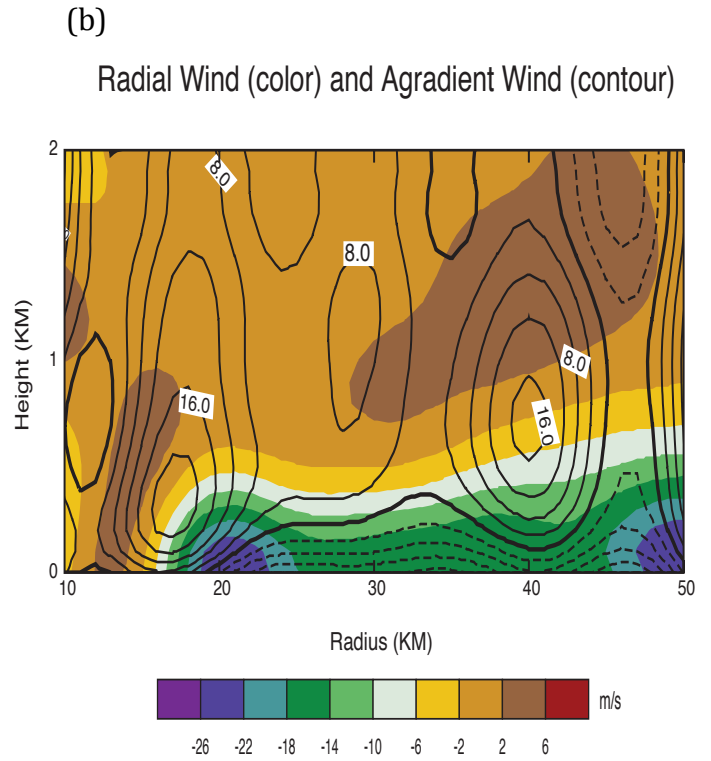
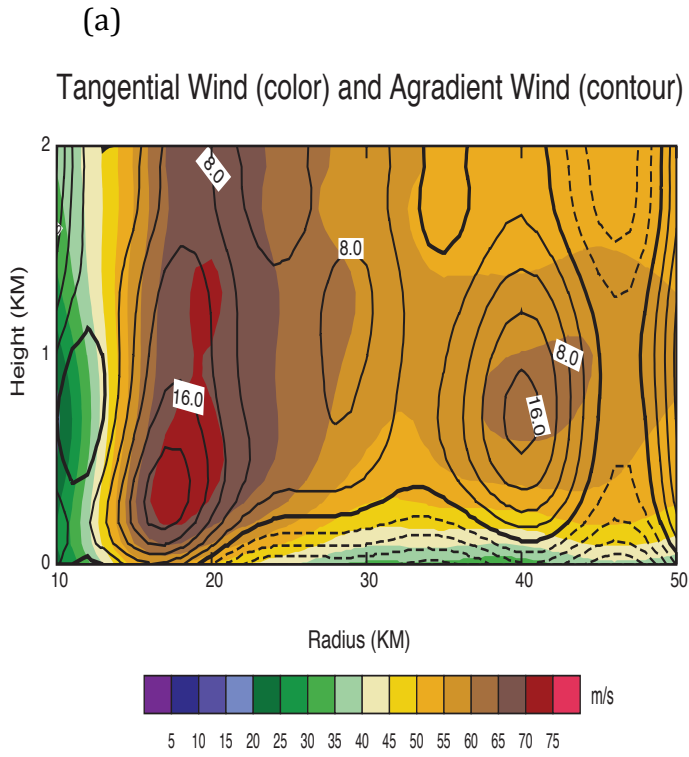


**Figure 4.7 Axisymmetric (a) tangential wind (color) and (b) radial wind (color). Axisymmetric SGW is contours in  $4 \text{ m s}^{-1}$  intervals. The bold black line indicates where SGW is  $0 \text{ m s}^{-1}$ , dashed lines are subgradient and solid lines are supergradient.**

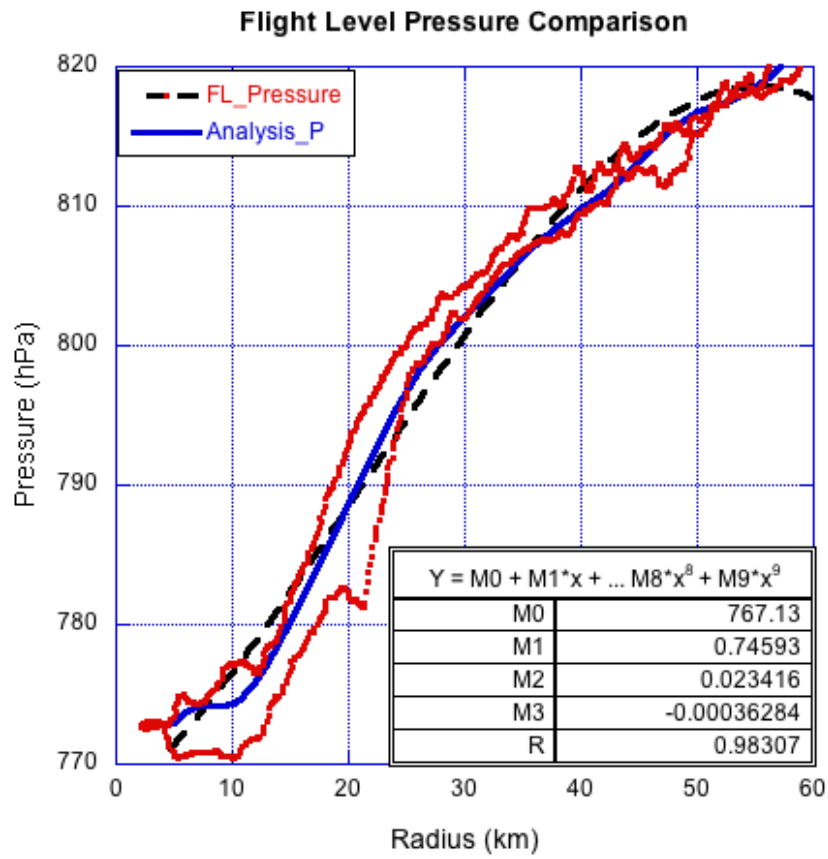


**Figure 4.8** Pressure with radius from north and south leg flight level in situ observations (red), axisymmetric SAMURAI analysis pressure (blue), and the axisymmetric pressure retrieved using the cubic polynomial method (black dashed). The box on the lower right has the equation and some statistics for the cubic polynomial fit.